

ARTICLE

Tumor cell heterogeneity drives spatial organization of the intratumoral immune response

Intratumoral heterogeneity (ITH)—defined as genetic and cellular diversity within a tumor—is linked to failure of immunotherapy and an inferior anti-tumor immune response. We modeled heterogeneous tumors comprised of "hot" and "cold" tumor populations (giving rise to T cell-rich and T cell-poor tumors, respectively) and introduced fluorescent labels to enable precise spatial tracking. We found the cold tumor cell population exerted a "dominant cold" effect in mixed tumors. Strikingly, spatial analysis revealed that the tumor cells themselves created distinct local microenvironments within heterogeneous tumors: regions occupied by cold tumor cells showed pronounced immunosuppression, harboring increased CD206^{Hi} macrophages and diminished local T cell function. This inferior T cell activity in cold regions persisted even after immunotherapy and mechanistically was mediated by CX3CL1 produced by the cold tumor cells. An immune cold tumor population within a heterogeneous tumor thus impairs tumor immunity on both a tumor-wide and a highly localized spatial scale.

Introduction

Immunotherapies have shown great promise in treating cancer by activating a patient's own immune cells to fight their tumor, but only a fraction of patients respond to current treatment regimens (Chen and Mellman, 2017; Darvin et al., 2018; Ribas and Wolchok, 2018; Das and Johnson, 2019). Immune checkpoint blockade (ICB) therapy routinely achieves durable cures in only a limited number of cancer types, and in many tumor types, response rates are as low as 15% with high relapse rates (Darvin et al., 2018; Das and Johnson, 2019). Genetic heterogeneity within a tumor is a significant factor that has been linked to poor ICB response (McGranahan et al., 2016; McGranahan and Swanton, 2017; Liu et al., 2019a). Tumors are often comprised of multiple populations of cancer cells, with each population carrying a distinct set of genetic alterations and phenotypic behaviors (Gerlinger et al., 2012; Turajlic et al., 2018; Hu et al., 2019). Genetic heterogeneity—often given the generalized label "intratumoral heterogeneity" (ITH)—is inherent in all cancer types (McGranahan and Swanton, 2017), and studies in multiple

cancer types have shown that tumors with high ITH are less likely to respond to ICB regimens (McGranahan et al., 2016; Liu et al., 2019a). In addition to genetic heterogeneity, tumors can also exhibit transcriptional heterogeneity—which can have genetic or nongenetic underpinnings—and recent evidence suggests that transcriptional heterogeneity itself can also limit anti-tumor immunity.

Mouse models of both genetic and transcriptional heterogeneity have begun to shed light on the mechanisms underlying the link between heterogeneity and an impaired anti-tumor immune response (Gejman et al., 2018; Li et al., 2018; Wolf et al., 2019; Westcott et al., 2023). In genetically heterogeneous tumors, differences in mutations result in differences in antigens between tumor cells. Genetically heterogeneous tumors thus harbor subclonal antigens present in some but not all tumor cells. Studies in models of melanoma, lung cancer, and colorectal cancer have demonstrated that the immune system mounts a poorer response to subclonal antigens than to clonal antigens,

¹Department of Microbiology and Immunology, University of California San Francisco, San Francisco, CA, USA; ²Department of Immunology, The University of Texas MD Anderson Cancer Center, Houston, TX, USA; ³The James P. Allison Institute, The University of Texas MD Anderson Cancer Center, Houston, TX, USA; ⁴Huntsman Cancer Institute, University of Utah, Salt Lake City, UT, USA; ⁵Department of Pathology, University of Utah, Salt Lake City, UT, USA; ⁶UCSF CoLabs, University of California San Francisco, San Francisco, CA, USA; ⁷Department of Cell and Tissue Biology, University of California San Francisco, San Francisco, CA, USA; ⁸Division of Hematology and Oncology, Department of Medicine, University of California San Francisco, CA, USA; ⁹Cancer Metabolism and Microenvironment Program, NCI-designated Cancer Center, Sanford Burnham Prebys Medical Discovery Institute, LA Jolla, CA, USA; ¹⁰ImmunoX Initiative, University of California San Francisco, CA, USA; ¹²Immunotherapy Integrated Research Center, Fred Hutchinson Cancer Center, Seattle, WA, USA; ¹³Department of Pathology, University of California San Francisco, CA, USA; ¹⁴Division of Gastroenterology, Department of Medicine, University of California San Francisco, CA, USA.

Correspondence to Melissa Q. Reeves: melissa.reeves@hci.utah.edu.

© 2025 Tanaka et al. This article is distributed under the terms as described at https://rupress.org/pages/terms102024/.





providing one mechanism by which ITH leads to inferior antitumor immunity (Gejman et al., 2018; Wolf et al., 2019; Nguyen et al., 2023; Westcott et al., 2023). Additionally, a study using mouse pancreatic ductal adenocarcinoma cell lines combined lines that gave rise to immune "hot" and immune "cold" tumors (defined as highly and lowly infiltrated by T cells, respectively). Mixing these cell lines resulted in an overall cold tumor, suggesting that coldness may be a dominant phenotype (Li et al., 2018). The two pancreatic ductal adenocarcinoma lines were presumed to have minimal mutational differences, and the effect was traced back to CXCL1 produced by cold tumor cells recruiting granulocytic suppressive myeloid cells (Li et al., 2018). These findings provide evidence that transcriptional heterogeneity in tumor cells can impair anti-tumor immunity by mechanisms orthogonal to those identified in antigen-heterogeneity studies.

Patients' tumors are frequently a patchwork of hot and cold regions (Abduljabbar et al., 2020; Mitra et al., 2020; Nirmal et al., 2022), indicating the anti-tumor immune response also exhibits spatial heterogeneity. One study of 85 pre-treatment lung cancers revealed that over two-thirds of tumors investigated contained both hot and cold regions (Abduljabbar et al., 2020). Further, a dysfunctional T cell phenotype can be spatially localized (Nirmal et al., 2022). However, model systems that lend themselves to mechanistically interrogating immunogenic heterogeneity within a tumor and its impact on the spatial organization of immune cells are limited at present. In the present study, we set out to ask not only how tumor heterogeneity impacts the immune response in the tumor as a whole but also to interrogate the relationship between tumor cell heterogeneity and the spatial organization of the intratumoral immune response.

Our studies employed tumor cell lines derived from carcinogen-induced squamous cell skin carcinomas induced by dimethylbenzanthracene and 12-O-tetradecanoylphorbol-13-acetate (DMBA/TPA) (Wong et al., 2013; Reeves et al., 2018). The DMBA/TPA skin carcinogenesis model gives rise to tumors that exhibit a physiologically relevant range of mutational burdens (averaging ~5 mutations/megabase; range: 0.7-21 mutations/ megabase) (McCreery et al., 2015; Nassar et al., 2015) and develop in immune-competent hosts, resulting in tumors with neoantigen and immune profiles that mimic those found in human tumors. We have generated cell lines from DMBA/TPAinduced tumors, which, when implanted into mice, give rise to tumors with reproducible immune phenotypes. Here, we develop a novel model of heterogeneous tumors by implanting a mixture of two such cell lines. Each cell line, labeled with a fluorophore, represents a distinct, trackable population within the tumor. The two cell lines we selected share a common oncogenic driver, Hras Q61L, but also each contain over 100 distinct nonsynonymous mutations. Additionally, these lines exhibit differences in tumor cell-produced chemokines and cytokines. Thus, their combination models a genetically and transcriptionally heterogeneous tumor.

Using this novel model system, we here interrogate the mechanisms by which heterogeneity in tumor cells impacts the immune response, the spatial organization of infiltrating immune cells, and the response to ICB therapy. We find, not surprisingly, that the presence of the tumor population that gives rise to cold tumors (hereafter, "the cold tumor population") drives an overall cold immune phenotype. The cold tumor population recruits an immunosuppressive microenvironment that dampens the overall immune response to the tumor as a whole but is particularly pronounced in the local vicinity of the cold tumor cells. We observe that our constituent tumor populations form a patchwork pattern within the tumor and that T cells in mixed-population tumors—although diminished in overall number—preferentially accumulate and exhibit superior effector function in the neighborhood of tumor cells that give rise to hot tumors (hereafter, "hot tumor cells"), while suppressive macrophages are especially abundant near cold tumor cells. Our study thus reveals that the spatial locations of tumor cell subpopulations create an architectural blueprint that profoundly influences the spatial localization and function of infiltrating immune cells. Furthermore, these patterns of spatial organization are not overcome by ICB treatment. Our model system of heterogeneity thus illuminates how heterogeneity in tumor cells impacts both the endogenous anti-tumor immune response and the efficacy of immunotherapy on a highly localized spatial scale.

Results

Modeling heterogeneous tumors with trackable tumor populations

We have established a series of squamous cell skin carcinoma cell lines, named the "carcinogen-induced tumor" (CIT) lines, derived from DMBA/TPA-induced skin carcinomas that were initiated in K5-CreERT2-Confetti mice on an FVB background (Reeves et al., 2018). To establish a model system in which to study the impact of tumor heterogeneity on the immune response, we selected and combined two of these cell lines, CIT6 and CIT9, that give rise, respectively, to tumors exhibiting a high and low frequency of overall T cells, CD4 T cells, and CD8 T cells, representing immunologically hot and cold tumors (Galon and Bruni, 2019). We introduced fluorescent labels into these tumor cells, taking advantage of CIT lines originating from mice carrying an unactivated Confetti cassette. We treated CIT6 and CIT9 with adenoviral Cre recombinase, leading to recombination of the Confetti allele and stochastic labeling of each cell with one of four fluorescent proteins-YFP, RFP, cyan fluorescent protein (CFP), and GFP (Snippert et al., 2010). We then sorted YFP+ cells from the CIT6 line and RFP+ cells from the CIT9 line to establish fluorescently tagged CIT6-YFP and CIT9-RFP cell lines. For subsequent experiments, these fluorescently labeled cell lines were implanted into syngeneic Confetti mice, carrying an unactivated Confetti allele, which recapitulated the expected hot and cold immune phenotypes we observed when unlabeled CIT6 and CIT9 tumor cells were implanted into wild-type FVB mice. We found that while the total infiltration of CD45⁺ immune cells was similar between CIT6-YFP and CIT9-RFP tumors (Fig. S1 A), we observed more total T cells, CD4 and CD8 T cells, B cells, and NKp46⁺ lymphocytes in CIT6-YFP tumors (Fig. 1, A–D and Fig. S1 B). By contrast, we found a higher infiltration of F4/80+ CD11b+



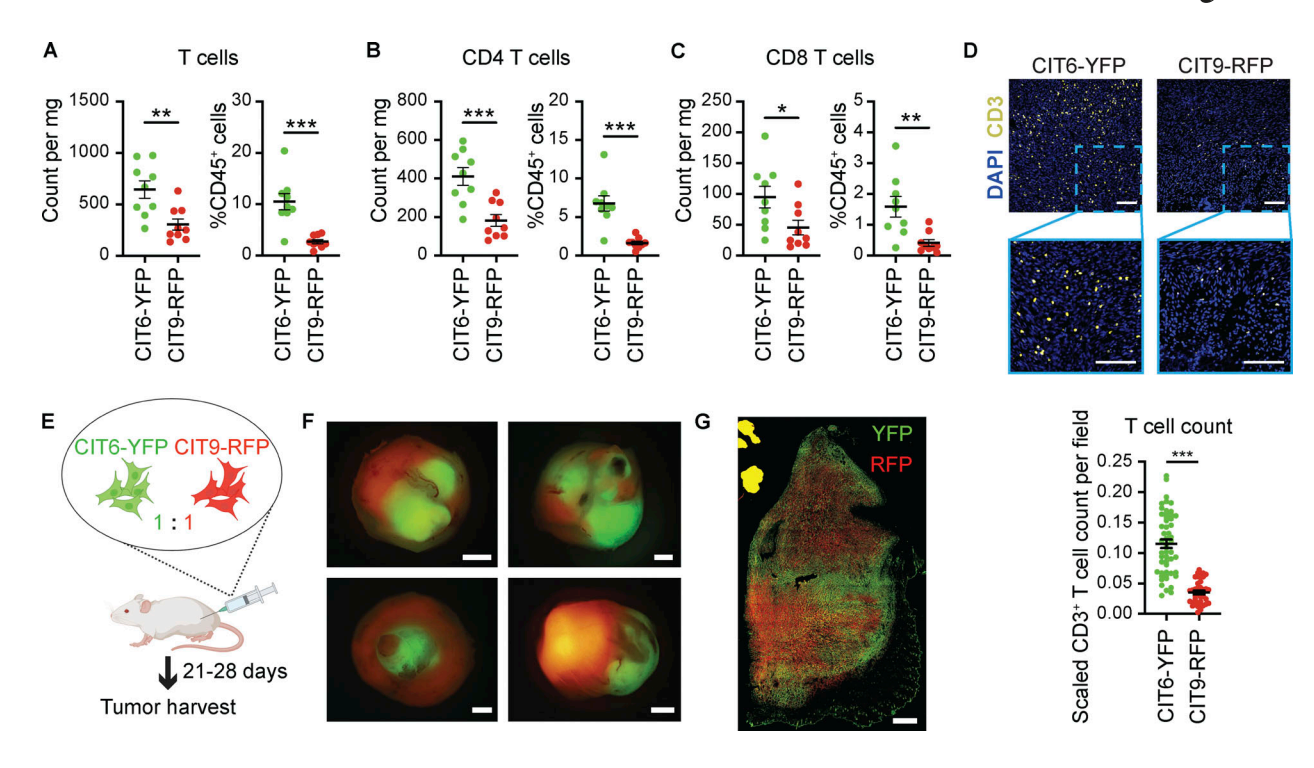


Figure 1. **Modeling ITH using fluorescently labeled DMBA/TPA-induced squamous cell skin carcinoma cell lines. (A–C)** Flow cytometric analysis of T cell infiltration in subcutaneous tumors derived from injection of CIT6-YFP and CIT9-RFP cell lines into mice carrying an unactivated *Confetti* cassette. n = 9. All data are a representation of at least three independent experiments. **(D)** IF staining of CD3⁺ T cells in 8- μ m cryosections of subcutaneous CIT6-YFP and CIT9-RFP tumors, with DAPI staining cell nuclei, and quantification of T cell count per field. Scale bar = 100 μ m. T cells were counted in 52 (CIT6-YFP) and 39 (CIT9-RFP) tiles in each arm. Data are a representation of two independent experiments. **(E)** Schematic of mixed-population tumor generation. A 1:1 mixture of CIT6-YFP and CIT9-RFP cell lines was subcutaneously injected into the right hind flank of mice carrying an unactivated *Confetti* cassette, and the resulting tumors were harvested for downstream analyses when they reached 1 cm in diameter at 21–28 days after injection. **(F and G)** Whole-tumor images by fluorescent dissecting microscope (F) and a representative image of a tumor cross-section (8- μ m cryosection) (G) of tumors that were a 1:1 mixture of CIT6-YFP and CIT9-RFP cell lines. Scale bars in F and G are 2 and 1 mm, respectively. Images are representation of >100 tumors we have analyzed throughout the experiments in the paper. Statistical significance was determined by Student's t test (A–D). *P < 0.05, **P < 0.01, and ***P < 0.001.

MHC-II⁺ macrophages, which often harbor immunosuppressive properties in the tumor microenvironment (TME) (DeNardo and Ruffell, 2019; Mehta et al., 2021), in CIT9-RFP tumors (Fig. S1 C). Thus, while we initially defined CIT6 as hot and CIT9 as cold based on high and low T cell infiltration, respectively, the abundance of other immune cell populations in each tumor is consistent with these labels.

To model heterogeneous tumors, we injected mice subcutaneously with an equal mixture of CIT6-YFP and CIT9-RFP cell lines $(6.25 \times 10^4 \text{ cells each, totaling } 1.25 \times 10^5 \text{ cells per injection})$ (Fig. 1 E). Tumors were assessed for composition by fluorescence stereomicroscopy at the time of harvest, when tumors were 1 cm in longest diameter (21-28 days). We consistently observed approximately two-thirds of the resulting tumors were comprised of both YFP+ and RFP+ cells with clearly defined YFP+ and RFP+ regions, whereas the remaining one-third consisted of only RFP+ cells in most cases or only YFP+ cells in rare cases (Fig. 1 F; and Fig. S1, D and E). The tumors that contained both YFP+ and RFP+ cells, termed "mixed-population tumors" herein, were used for downstream analyses. When the equal mixture of CIT6-YFP and CIT9-RFP cells was implanted into immunodeficient NOD/SCID/ IL-2Ry null mice, which lack T, B, and natural killer (NK) cells and innate lymphoid cells, we observed a higher penetrance of mixed-population tumors, while by contrast we observed a

slightly lower penetrance of fluorescently labeled mixed-population tumors when FVB/N mice, rather than Confetti mice, were used as hosts (Fig. S1, D and E). This indicates that immune activity against tumor cells was likely responsible for cases where mixed tumors failed to establish. Inspection of the mixed-population tumors in Confetti mice by cryosectioning and fluorescent imaging showed a patchwork of regions that could be classified as being occupied primarily by YFP+ cells, primarily by RFP+ cells, or by a mixture of both populations (Fig. 1 G). The fluorescent tags in these cell lines thus successfully enabled spatial tracking and quantification of each tumor population in the mixed-tumor population tumors and enabled us to establish a novel model to study ITH.

An immunosuppressive phenotype dominates the immune microenvironment of mixed-population tumors

To determine how each constituent tumor population affects the overall immune response in mixed-population tumors, we performed a comprehensive flow cytometric analysis of the immune infiltrates (Fig. S1 F) found in CIT6-YFP + CIT9-RFP mixed-population tumors and compared this to infiltrates found in each CIT6-YFP and CIT9-RFP single-population (homogeneous) tumor. Mixed-population tumors have an overall cold immune phenotype, exhibiting CD4 and CD8 T cell infiltration



comparable with CIT9-RFP homogeneous tumors and significantly lower than that found in CIT6-YFP homogeneous tumors (Fig. 2 A). MHC-I proteins were expressed on >85% of CIT6-YFP and CIT9-RFP tumor cells and expressed at a similar level (Fig. 2 B), suggesting that the differences in T cell abundance are not due to the differences in MHC-I expression. MHC-II expression was very low on both CIT6-YFP and CIT9-RFP tumor cells (Fig. S2 A). Although there was no significant difference in the fraction of CD4 T cells that were regulatory T cells (Tregs; CD4+ CD25+ Foxp3+) or in the CD8 T cell-to-Treg ratio between any of the groups, CIT9-RFP and mixed-population tumors showed a lower CD4 effector T cell (Teff) (CD4+ CD25- Foxp3-)-to-Treg cell ratio than CIT6-YFP tumors (Fig. 2 C). Other lymphocytes, specifically B cells and NKp46+ lymphocytes (including NK cells and innate lymphoid cells), showed a similar pattern: mixedpopulation tumors overall resembled the low lymphocytic infiltration pattern of CIT9-RFP tumors (although the difference between NKp46+ lymphocytes in CIT6-YFP versus mixed tumors was not statistically significant) (Fig. 2 D).

Mixed-population tumors had an increase in CD11b⁺ myeloid cells and a trend toward more macrophages compared with CIT6-YFP tumors, again exhibiting more similarity in immune profile to CIT9-RFP tumors (Fig. 2 E and Fig. S2 B). Macrophages are conventionally known to facilitate antigen presentation and assist in T cell activation, but in the context of a tumor, evidence suggests that tumor-associated macrophages (TAMs) are more frequently a mediator of immunosuppression (DeNardo and Ruffell, 2019). TAMs are the most abundant immune cells in CIT6-YFP and CIT9-RFP tumors, comprising 30-80% of total CD45⁺ immune cells. Therefore, we sought to determine if F4/ 80+ CD11b+ MHC-II+ macrophages in our tumors are functionally immunosuppressive. Macrophages were sorted from CIT6-YFP, CIT9-RFP, and mixed-population tumors and assessed for their capacity to suppress CD8 T cells isolated from naïve, non-tumorbearing syngeneic Confetti mice and activated by CD3/CD28 beads. In comparison to CD8 T cells alone, the addition of TAMs significantly suppressed CD8 T cell proliferation, measured as the number of cells that had undergone division (as marked by CFSE dilution) (Fig. 2 F). The expansion of activated T cells, measured as CD69+ CD25+ CD8+ T cells (early activation), CD69-CD25+ CD8+ T cells (late activation), or PD-1+ CD8+ T cells, showed similar results, whereby the addition of macrophages decreased the number of activated T cells (Fig. 2 G and Fig. S2 C). Moreover, the expansion of the CD62L- CD44+ Teff subset and the CD62L+ CD44+ central memory T cell subset was significantly suppressed in the presence of TAMs (Fig. 2 H and Fig. S2 D). Thus, we conclude that macrophages in our CIT tumors are indeed functionally immunosuppressive and contribute toward a suppressive TME. Ly6G+ Ly6Cmid neutrophils, Ly6G-Ly6C+ monocytes, and CD11b+ CD11c+ MHC-II+ F4/80- dendritic cells (DCs) showed a similar abundance across all tumors (Fig. S2 E). Collectively, these data reveal that the immunosuppressive phenotype is dominant in mixed-population tumors.

To determine if CIT9 tumor cells could exert this dominant cold influence when present as a minor population, we implanted mice with tumors containing increasing ratios of CIT6: CIT9 tumor cells, specifically, 1:1, 3:1, or 9:1 ratios (50%, 25%, or

10% cold tumor cells). Of note, this particular experiment was carried out with CIT6 and CIT9 parental cell lines lacking YFP and RFP fluorophores. We observed that 1:1, 3:1, and 9:1 CIT6: CIT9 mixed tumors all exhibited T cell infiltration that was significantly lower than CIT6 homogeneous controls and not significantly different than CIT9 homogeneous controls (Fig. 2 I). We thus conclude that cold CIT9 cells are able to exert a dominantly immunosuppressive effect on the TME even when present only as a minor population.

Spatial organization of tumor populations drives the spatial organization of immune cells

Since the mixed-population tumors were comprised of a patchwork of YFP, mixed, and RFP tumor regions, we next sought to better understand whether the "dominant cold" immune phenotype was uniformly true in all tumor regions. To this end, we first quantified CD3+ T cells by immunofluorescent (IF) staining of 8-µm sections. We classified each field of view as predominantly occupied by CIT6-YFP cells ("YFP regions"; >60% of tumor cells are YFP+), predominantly occupied by CIT9-RFP cells ("RFP regions"; >60% of tumor cells are RFP+), or mixed ("mixed regions"; YFP and RFP each represent >40% of tumor cells) and then quantified the number of CD3+T cells in the field (Fig. 3 A). This analysis revealed a significantly higher average count of CD3+ T cells in YFP regions compared with RFP regions, with mixed regions showing an intermediate level (Fig. 3 B). Further, we observed a significant positive correlation between the number of T cells and the fraction of YFP tumor cells (R^2 = 0.22, $P = 4.7 \times 10^{-35}$) in each field and noticed that the fields of view with the highest number of infiltrating T cells were all comprised of >50% YFP+ cells (Fig. 3 C). These data suggest that T cells preferentially localize to the regions occupied by CIT6-YFP tumor cells in mixed-population tumors.

We next turned to flow cytometry-based analysis of the immune cells in each YFP, mixed, and RFP regions to gain a higher dimensional profile of the immune response in each region. Mixed-population tumors were embedded into agarose gel, and each tumor was sliced into five to ten 400-µm-thick live sections. Each section was manually microdissected into YFP, mixed, and RFP regions using a surgical scalpel under a fluorescent dissecting microscope. All YFP pieces, all mixed pieces, and all RFP pieces from the same tumor were pooled and digested into a single-cell suspension for immune profiling by flow cytometry (Fig. 3 D). While a similar frequency of total CD45+ immune cells was observed in all three regions (Fig. S2 F), we found a higher frequency of total CD3+ T cells in YFP regions than in RFP regions (Fig. 3 E and Fig. S2 G), mirroring our findings by IF. This localization pattern was also seen in, and was driven by, CD4 T cells (Fig. 3 F and Fig. S2 G). By contrast, CD8 T cells were at low abundance in all regions of mixed tumors, including YFP regions, and were found at levels resembling those in single-population CIT9-RFP tumors (Fig. 3 G). A more detailed analysis of T cell function showed that nearly onethird of the CD4 T cells in YFP regions were Th1 cells (CD4+ IFN γ^+), whereas only ~2% of CD4 T cells in RFP regions were Th1 cells (median frequency of T helper [Th]1 cells in YFP regions = 28.9%, RFP regions = 1.99%) (Fig. 3 H). Th2 (CD4+ IL-4+) and Th17



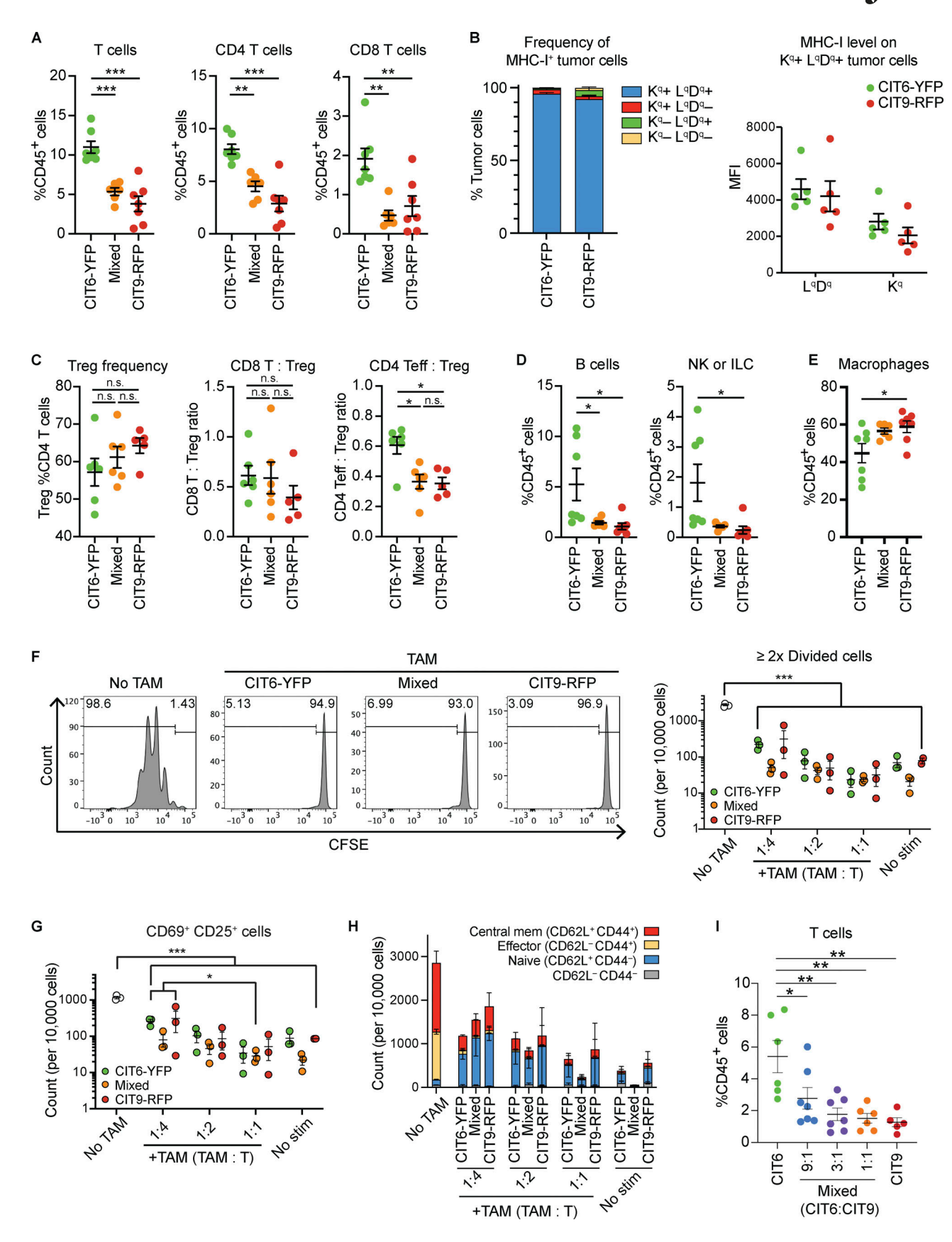


Figure 2. The cold tumor population drives an overall immunosuppressive phenotype in mixed-population tumors. (A–E) Flow cytometric immune profiling of single-population (homogeneous) CIT6-YFP and CIT9-RFP tumors and 1:1 mixed-population tumors, including (A) T cells, CD4 T cells, and CD8 T cells (n = 6–7), (B) frequency of tumor cells (CD45⁻ YFP⁻ or CD45⁻ RFP⁻) expressing MHC-I molecules (H2-K^q and H2-L^qD^q) (left) and median fluorescence



intensity (MFI) of the MHC-I molecules on H2-Kq and H2-LqDq double-positive tumor cells (right) (n = 5), (C) Treg (Foxp3+ CD25+) frequency, CD8 T cell-to-Treg ratio, and Teff (Foxp3- CD25-)-to-Treg ratio (n = 5-6), (C) B cells (B220+) and NK or innate lymphoid cell (ILC) (NKp46+) lymphocytes (C) lymphocytes (C) and (C) macrophages (F4/80+ CD11b+ MHC-II+) (C) (C) Data in A-E are a representation of at least two independent experiments. (C) In vitro CD8 T cell suppression by macrophages sorted from the tumors. CFSE-stained and CD3/28 beads-stimulated CD8 T cells isolated from naïve C for proliferation via CFSE signal and activation markers. Data are a representation of two independent experiments, with three biological replicates in each experiment. (C) Representative histogram showing the CFSE signal in CD8 T cells, with gates marking divided cells defined as cells having undergone C0 divisions, in no TAM condition or 1:1 TAM:T cell ratio (50K T cell + 50K TAM conditions) (left), and graph showing the count of divided cells (right). "No TAM," T cell stimulation control without macrophages; "No stim," control with no T cell stimulation. (C0 Count of activated (CD69+ CD25+) CD8 T cells. (C1) Count of effector CD8 T cell subsets marked by combinations of CD62L and CD44 expression. (C1) Flow cytometric analysis of T cell infiltration in mixed-population tumors derived from varying ratios of CIT6:CIT9 cell lines. C1 Statistical significance was determined by one-way ANOVA (C2 and C3) or two-way ANOVA (C4.) with Tukey's correction posttest. C6 over C7 and C8.

(CD4* IL-17*) cells were equally rare in all regions (Fig. 3 I). Even more strikingly, despite their low abundance, CD8 T cells showed increased effector function in YFP regions: over 70% of CD8 T cells in YFP regions showed the capacity to produce IFNy, whereas <10% of CD8 T cells in mixed and RFP regions showed the same (Fig. 3 J). There was no apparent difference in Treg (Foxp3* CD25*) cell frequency between regions (Fig. 3 K), but the ratio of Treg:Th1 cells and Treg: IFNy* CD8 T cells was higher in RFP regions compared with YFP and mixed regions (Fig. 3 L). In addition, macrophages (F4/80* CD11b* MHC-II*) were significantly enriched in mixed regions and RFP regions compared with YFP regions (Fig. 3 M and Fig. S2 H).

Collectively, these data show that local tumor cells themselves play a significant role in driving the immune microenvironment in their vicinity. Moreover, the observation that T cell effector marker expression and macrophage infiltration in mixed regions look similar to RFP regions suggests that in regions in which both CIT6-YFP and CIT9-RFP tumor cells coexist, cold CIT9-RFP tumor cells exert a dominant suppressive influence. The "dominant coldness" of CIT9-RFP is also seen in the global suppression of CD8 T cell infiltration in all regions. CIT9-RFP tumor cells thus impair the T cell response in mixed tumors in two ways: first, by blunting the overall CD8 response in all regions; and second, by creating spatially localized pockets where both CD8 and CD4 T cells exhibit virtually no effector function.

A cold tumor population drives resistance of mixed-population tumors to immunotherapy

Having shown that CIT9-RFP tumor cells in mixed-population heterogeneous tumors exert a dominant immunosuppressive effect and drive spatial organization of immune cells within the tumor, we next sought to determine how the presence of CIT9-RFP tumor cells would impact the response of mixed-population tumors to ICB therapy. We treated tumors with a regimen combining PD-1 blockade and CD40 agonist antibodies, a combination that is currently in clinical trials for multiple tumor types. The combination treatment was administered in two doses at a 3-day interval when tumors reached 5 mm in diameter (Fig. 4 A) and was effective in controlling homogeneous CIT6-YFP tumors but not homogeneous CIT9-RFP tumors (Fig. 4 B). We observed 50% of CIT6-YFP tumors (5 out of 10 tumors) regressed completely, with two tumors eventually growing back after 5-17 days (Fig. 4 B). In contrast, only 1 out of 11 of CIT9-RFP

tumors showed a decrease in tumor volume after therapy, and none (0 out of 11) achieved a complete regression (CR) (Fig. 4 B). Furthermore, treatment successfully blunted the growth of CIT6-YFP tumors and prolonged survival of mice-bearing CIT6-YFP tumors, but neither of these was achieved in CIT9-RFP tumors (Fig. 4, B and C). ICB treatment was thus effective in hot, but not cold, homogeneous tumors. Immune profile analysis further revealed that CD4 and CD8 T cell infiltration was increased in CIT6-YFP tumors, but not in CIT9-RFP tumors (Fig. 4 D).

We next assessed the response of tumors derived from a 1: 1 mixture of CIT6-YFP and CIT9-RFP cell lines to the same ICB regimen. The combination therapy achieved CR in 1 out of 23 mice (4.3%), but the tumor quickly grew back (Fig. 4 E). The therapy had a statistically significant but modest effect on the overall growth of mixed tumors and did not prolong overall survival for mice-bearing mixed tumors (Fig. 4, E and F), overall demonstrating less efficacy in mixed tumors than homogeneous CIT6-YFP tumors. Interestingly, we observed an influx of T cells into mixed tumors treated with therapy (Fig. 4 G), but this influx did not correspond to the same rate of CRs seen in CIT6-YFP tumors. Collectively, these data suggest that the presence of CIT9-RFP tumor cells dampens the response of mixed tumors to the combination treatment and also reveal that an improved influx of T cells into the tumor after treatment is not necessarily a marker of a successful response in the context of a heterogeneous tumor. We also quantified tumor-infiltrating myeloid cells and observed no change in tumor-infiltrating macrophages following treatment in any tumor cohort (Fig. S2, I-K).

Spatial immune infiltration patterns persist in mixedpopulation tumors following anti-PD-1 blockade and CD40 agonist combination treatment

Given our previous data showing that RFP regions (and to a lesser extent, mixed regions) of mixed-population tumors were spatially organized pockets of immune coldness, we sought to test the hypothesis that the immunotherapy combination treatment was failing to overcome the cold TME surrounding CIT9-RFP tumor cells. We applied our live tumor slice microdissection technique (Fig. 3 D) to mixed-population tumors treated with either anti-PD-1 blockade + CD40 agonist or control antibodies and analyzed the immune infiltration profiles of YFP, RFP, and mixed regions 6 days after the initial treatment dose, at



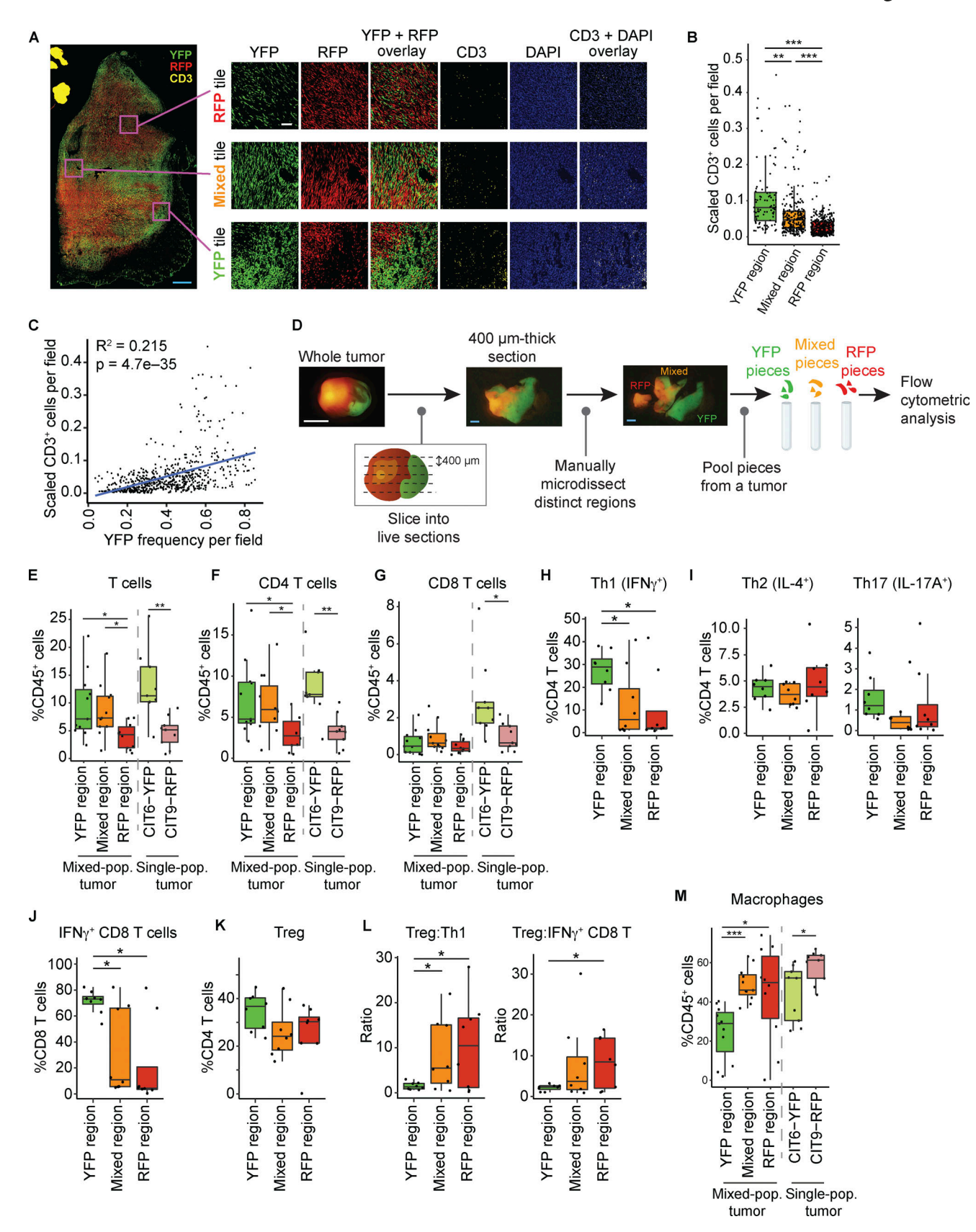


Figure 3. **Spatial organization of tumor populations drives the spatial organization of immune cells. (A)** Cross-section images showing examples of a YFP, mixed, and RFP region of a mixed-population tumor and CD3 stain. The image is representation of at least seven tumors. Blue scale bar = 1 mm, white scale bar = 100 μ m. **(B)** Quantification of CD3⁺ T cells per field, plotted for each region. The data are a representation of eight tumors analyzed in two independent experiments. **(C)** Correlation of YFP⁺ cell fraction and CD3⁺ T cell frequency in each field. CD3⁺ T cell count was scaled to DAPI⁺ cell count in each



field to normalize the difference in cell density between fields. The data are a representation of eight tumors analyzed in two independent experiments. **(D)** Schematic of immune cell profiling in YFP, mixed, and RFP regions of mixed-population tumors. Each mixed-population tumor was sliced into five to ten 400- μ m-thick live sections, and each section was manually microdissected into YFP, mixed, and RFP regions using a surgical scalpel under a fluorescent dissecting microscope. All YFP pieces, all mixed pieces, and all RFP pieces from the same tumor were pooled for immune profiling by flow cytometry. White scale bar = 5 mm, blue scale bar = 1 mm. **(E-M)** Frequency of T cell subsets, ratio of Treg to IFNy+ CD8 T cells or Th1 cells, and frequency of macrophages in YFP, mixed, and RFP regions. Grey dotted lines in panels E–G and M separate data of mixed-population tumors from the data of single-population tumors. Data are a representation of two independent experiments with \geq 6 mice per experiment. Statistical significance was determined by Student's t test (B and E–M) or Pearson's correlation test (C). *P < 0.05, **P < 0.01, and ***P < 0.001.

which point tumors have not started to shrink yet (Fig. 5, A and B).

At the 6-day time point, the frequencies of overall CD4 and CD8 T cells did not differ between the isotype control arm and the combination treatment arm in any of the three regions (Fig. S2 L). However, the abundance of Th1 cells was increased in RFP and mixed regions of ICB-treated tumors and showed a trend toward increasing in YFP regions (Fig. 5 C). The treatmentinduced change in abundance was unique to Th1 cells, as other CD4 T cell subsets, including Treg, Th2, and Th17 cells, showed a similar frequency between isotype control and combination treatment arms (Fig. 5, D and E). The changes in Th1 cell abundance resulted in a favorable increase in the Th1:Treg ratio in mixed and RFP regions of the combination therapy-treated tumors (Fig. 5 F). The functional impact on the CD8 T cell compartment was less dramatic (Fig. 5, G and H). Strikingly, however, in both the CD4 and CD8 compartments, the spatial segregation of the immune response—characterized by more Th1 and IFNγ⁺ CD8 T cells in YFP regions—was preserved after therapy (Fig. 5, C and G). The improvements in RFP regions, although in some cases statistically significant, were of small magnitude on an absolute scale. Collectively, these data show that anti-PD-1 and CD40 agonist antibody treatment was successful at improving the overall quality of the intratumoral immune response, but the abundance of Teffs in RFP regions remained inferior to that in YFP regions. As a result, ICB therapy could modestly slow tumor growth but was largely insufficient to mediate tumor rejection.

CD206^{Hi} macrophages and lack of neutrophils and inflammatory monocytes are associated with the immunosuppressive TME of RFP regions

Having observed that CIT9-RFP tumor cells were able to establish local regions of poor T cell activity in their immediate vicinity and that these regions persisted even after immunotherapy, we next sought to understand the mechanism driving this diminished T cell activity in RFP regions. To do so, we employed ZipSeq spatial transcriptomics (Hu et al., 2020) to CIT6-YFP + CIT9-RFP mixed-population tumors. ZipSeq allows immune cells within user-defined regions of interest in live tissue sections to be tagged with distinct nucleotide sequences (akin to assigning each region of interest a unique zipcode), making use of photocaged oligonucleotides and precise light exposure. Using this method, immune cells from YFP, RFP, and mixed regions of mixed-population tumors (n = 2) were tagged with distinct "zipcode" barcodes, and sections were subsequently disaggregated and subjected to single-cell RNA sequencing (scRNA-seq) (Fig. 6 A). Immune cells were subjected to

uniform manifold approximation and projection UMAP) clustering, and cluster identities were assigned based on expression of well-established markers (Fig. 6 B and Fig. S3, A-C). Using ZipSeq barcodes, we mapped each immune cell back to the region it originated from (Fig. 6 C). In line with our flow cytometry analyses, we observed a higher infiltration of T cells in YFP regions compared with RFP regions (Fig. 6 D) and also saw that myeloid cells comprised a majority of the immune cells (Fig. 6 B). Strikingly, we observed that the majority of macrophage clusters (four out of five) were enriched in RFP regions including three of which were in the top four largest clusters overall (macrophage-1, -2, and -3) (Fig. 6 E). By contrast, neutrophils and inflammatory monocytes were observed at lower abundance in RFP regions than YFP regions (Fig. 6, F and G). We carried out ZipSeq single-cell spatial transcriptomics on a second mixed-population tumor and found similar results (Fig. S3, D-K): myeloid cells comprised a majority of the immune cells (Fig. S3, D-G), T cells were enriched in YFP regions (Fig. S3 H), the majority (six of seven) macrophage clusters were enriched in RFP regions (Fig. S3 I), and neutrophils and inflammatory monocytes were enriched in YFP regions (Fig. S3, J and K). Pathway analysis with EnrichR, using genes enriched in each cluster and the Gene Ontology (GO) Biological Process 2021 repository, suggested neutrophils had pro-inflammatory properties, as seen by neutrophil activation-related genes (Fig. 6 F and Fig. S3 J). Monocytes also exhibited evidence of activation, with a particularly clear pro-inflammatory signature in the second tumor (Fig. 6 G and Fig. S3 K).

Given the striking enrichment in macrophages in tumor regions occupied by CIT9-RFP tumor cells, we next sought to determine if a particular macrophage subset might be responsible for the poor T cell activity observed in these regions. We observed multiple macrophage clusters expressing Mrc1 (CD206) and Arg1 (Fig. S3, C and L), both of which are markers frequently associated with suppressive TAMs. The ZipSeq experiments carried out in two tumors did not allow us to pinpoint if a specific macrophage subset was consistently enriched in RFP tumor regions, so we turned to our microdissection plus flow cytometry workflow (Fig. 3 D) to analyze the macrophages in each region in a larger cohort of tumors. Macrophages were classified as CD206Hi (CD206Hi MHC-IILow), Arg1Hi (CD206Mid MHC-II^{Hi} Arg1+), and MHC-II^{Hi} (CD206Mid MHC-II^{Hi} Arg1-) (Fig. S4 A). Consistent with previous experiments, we found macrophages were more abundant in RFP regions than YFP regions (Fig. 6 H). Strikingly, this difference was driven specifically by CD206Hi macrophages, which were most abundant in RFP regions, least abundant in YFP regions, and of intermediate abundance in mixed regions (Fig. 6 I). Arg1Hi and MHC-IIHi



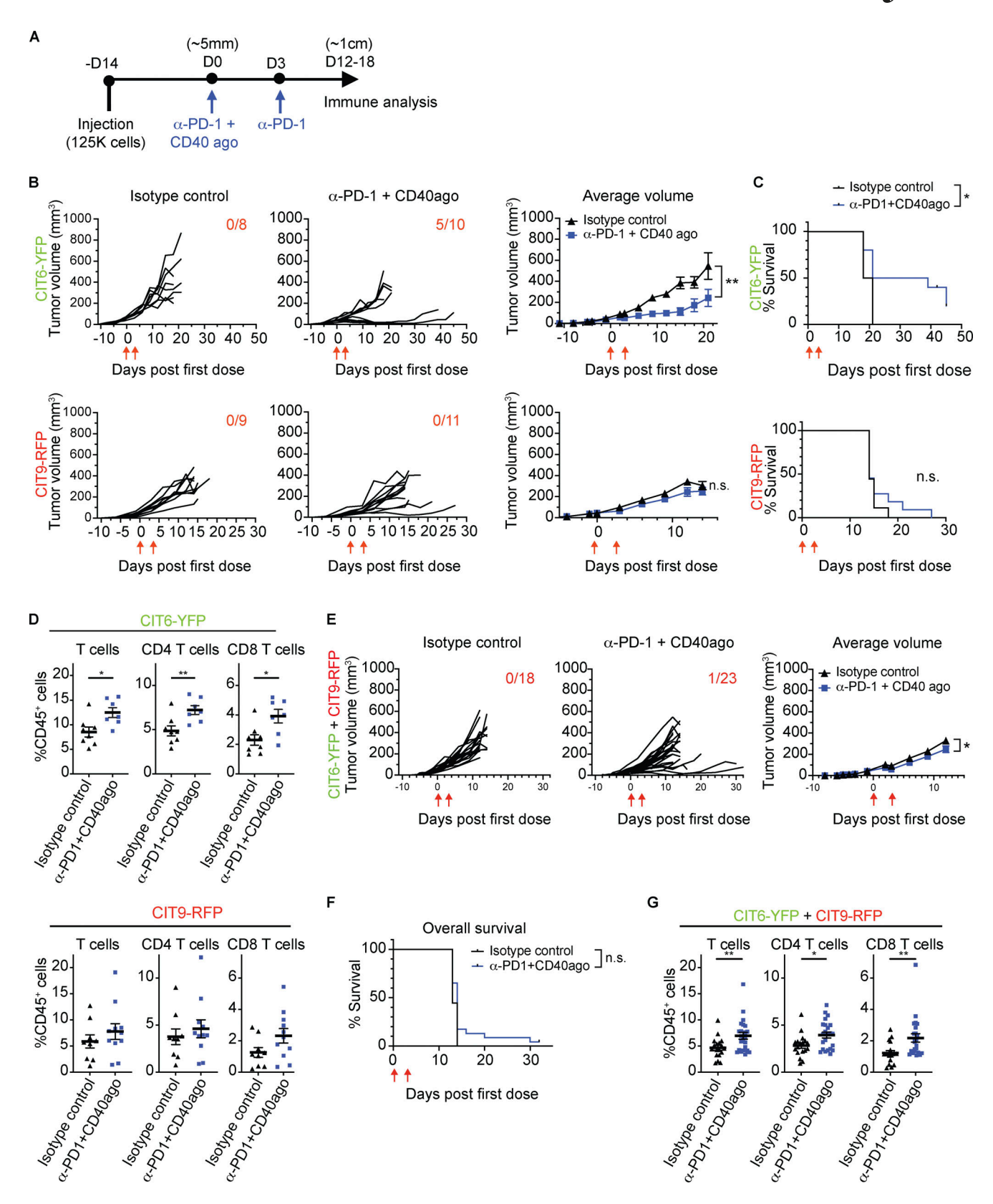


Figure 4. A cold tumor population drives resistance of mixed-population tumors to anti-PD-1 blocking and CD40 agonistic antibody combination treatment. (A) Dosing schedule of anti-PD-1 and CD40 agonist treatment. (B) Tumor growth curves of CIT6-YFP and CIT9-RFP tumors showing tumor volume of individual tumors and average volume of isotype control and anti-PD-1 + CD40 agonist combination treatment arms. Red arrows under the x axis shows the timing of treatments (day [D]0 and 3), fraction shown on the top right corner of individual tumor volume plots shows the number of mice whose tumors completely regressed after treatment. n = 8-11. (C) Kaplan-Meier curves comparing the survival of mice from each treatment arm. Statistical test was performed using log-rank test. (D) Frequency of tumor-infiltrating T cells after treatment in CIT6-YFP and CIT9-RFP tumors. n = 7-11. (E and F) Tumor growth



and survival of mice harboring tumors derived from a 1:1 mixture of CIT6-YFP and CIT9-RFP cell lines. n = 18-23. (G) Frequency of tumor-infiltrating T cells after treatment in 1:1 mixture-derived tumors. n = 18-23. All experiments were performed once. Statistical significance was determined by two-way ANOVA (B and E) or Student's t test (D and G), and Kaplan–Meier survival analyses were performed by log-rank (Mantel–Cox) test (C and F). *P < 0.05 and **P < 0.01.

macrophages by contrast were not different in abundance between regions in terms of total frequency (Fig. 6 I), although they made up a smaller relative proportion of macrophages in RFP regions (Fig. S4 B).

Given the low abundance of T cells in RFP regions, we next asked whether CD206^{Hi} macrophages had a greater capacity to suppress T cell proliferation than non-CD206^{Hi} macrophages (which include both MHC-II^{Hi} and Arg1^{Hi} macrophages). We isolated CD206^{Hi} and non-CD206^{Hi} macrophages from CIT9-RFP and CIT6-YFP tumors by flow cytometry-based sorting (Fig. S4 A) and tested for their ability to suppress CD8 T cell proliferation using an in vitro co-culture assay. We found that CD206^{Hi} macrophages could suppress T cell proliferation and activation

even at a low macrophage-to-CD8 T cell ratio (1:16), whereas non-CD206^{Hi} macrophages could suppress CD8 T cells only at a higher co-culture ratio (1:4) (Fig. 6 J and Fig. S4 C). Thus, while both CD206^{Hi} and non-CD206^{Hi} macrophages exhibited suppressive capacity to some extent, the CD206^{Hi} macrophage subset in our tumors—which is preferentially enriched in RFP tumor regions—has a particularly strong ability to suppress T cell proliferation.

Chemokine CX3CL1 is a mediator of the CIT9-RFP-driven immunosuppressive TME

To identify the drivers behind the striking spatial organization of myeloid cell infiltrates in our mixed tumors, we next assessed

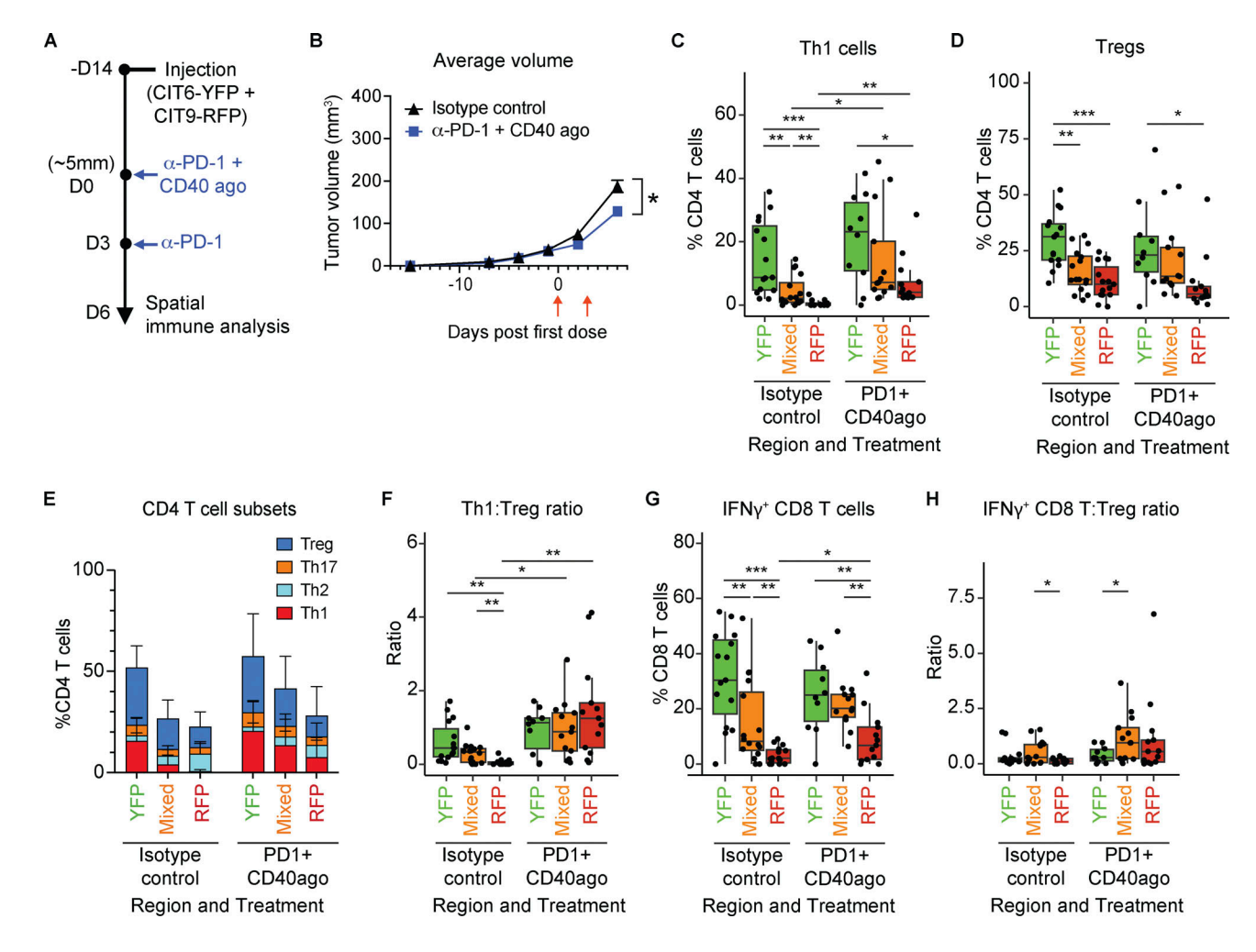


Figure 5. Spatial immune infiltration patterns persist in mixed-population tumors following anti-PD-1 blockade and CD40 agonist combination treatment. (A) Schematic of tumors derived from a 1:1 mixture of CIT6-YFP and CIT9-RFP cell lines treated with anti-PD-1 + CD40 agonist combination treatment or isotype control antibodies at days (D)0 and 3 and subject to spatial analysis of T cell infiltration at day 6. (B) Average tumor volume of each treatment arm. Red arrows under the x axis shows the timing of treatments. n = 19-23. (C-H) Flow cytometric analysis of T cell subsets in each region of isotype control-treated and combination therapy-treated tumors, showing Th1 cell frequency (C), Treg frequency (D), frequency of all CD4 T cell subsets (E), Th1-to-Treg ratio (F), frequency of IFNy+ CD8 T cells (G), and IFNy+ CD8 T cell-to-Treg ratio (H). n = 10-16. All experiments were performed once. Statistical significance was determined by two-way ANOVA with Tukey's correction posttest (B) or Student's t test (C-H). *P < 0.05, **P < 0.01, and ***P < 0.001.



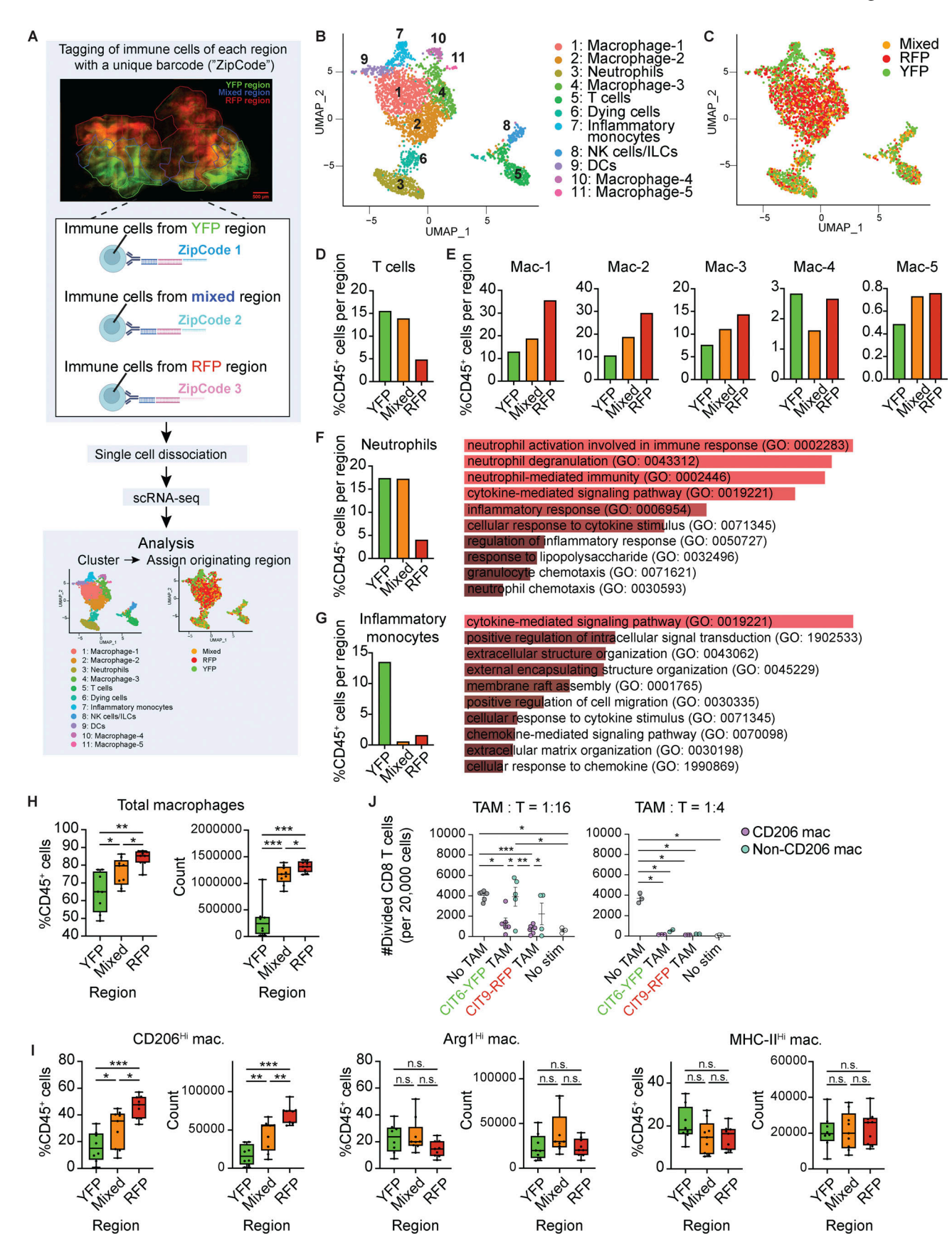


Figure 6. CD206^{Hi} macrophages and a lack of neutrophils and inflammatory monocytes are associated with an immunosuppressive TME in RFP regions. (A) Schematic of ZipSeq spatial transcriptomic analysis of mixed-population tumors. Composite stitched image of a 200-μm-thick live section marked



with YFP regions (encircled with green lines), RFP regions (red lines), and mixed regions (blue lines) is shown. YFP, RFP, and mixed regions were illuminated individually to allow for the binding of a unique barcode ("zipcode") to a photocaged oligo-CD45 antibody complex. Zipcode-tagged immune cells were analyzed by scRNA-seq. (B) UMAP representation of zipcode-labeled cells with cluster overlay. n = 3,238 cells. (C) UMAP representation of zipcode-labeled cells with zipcode identity overlaid. $n_{YFP} = 1,236$, $n_{RFP} = 1,318$, and $n_{Mixed} = 684$. (D) Abundance of cells belonging to the T cell cluster (cluster 5), calculated as percentage of total immune cells in each region. (F) Percentage of cells belonging to neutrophil cluster (cluster 3) in each region and pathway analysis showing the gene families enriched in the neutrophil cluster based on the top 250 differentially expressed genes. (G) Percentage of cells belonging to inflammatory monocyte cluster (cluster 7) and pathway analysis of genes enriched in the monocyte cluster based on the top 31 differentially expressed genes. Data in D-G are a representative data of one tumor out of two tumors analyzed. (H and I) Frequency of total macrophages (H) and three macrophage subsets (see Fig. S4 A for gating scheme) (I) detected by flow cytometric analysis in microdissected YFP, mixed, and RFP regions. n = 8-9. The experiment was performed once. (J) CD8 T cell suppression assay using CD206^{Hi} macrophages and non-CD206^{Hi} macrophages (combined Arg1^{Hi} and MHC-II^{Hi} macrophages) isolated from CIT6-YFP and CIT9-RFP single-population tumors. n = 3-6. Data are a representation of two independent experiments. Statistical significance was determined by one-way ANOVA (H and I) or two-way ANOVA (J) with Tukey's correction posttest. *P < 0.05, **P < 0.01, and ***P < 0.001. ILC, innate lymphoid cell.

the protein expression of a total of 44 cytokines and chemokines using the lysates from CIT6-YFP and CIT9-RFP tumors. Cytokines and chemokines are major mediators of immune cell localization and function; thus, we hypothesized differences in their expression between CIT6-YFP and CIT9-RFP might explain the differences we saw in myeloid infiltrate. We found the chemokine CX3CL1 was significantly enriched in CIT9-RFP tumors compared with CIT6-YFP tumors (Fig. 7 A and Fig. S4 D). CX3CL1 is a chemokine with reported pro-tumor properties, capable of directly promoting tumor cell proliferation and migration as well as of attracting various immune cell types through its cognate receptor, CX3CR1 (Conroy and Lysaght, 2020; Korbecki et al., 2020). Using our ZipSeq dataset, we assessed the correlation between the Cx3cr1 expression level in immune cells and their abundance in RFP regions. Cx3cr1 transcript level was high in clusters that were enriched in RFP regions and particularly high in many macrophage clusters (Fig. S5, A and B). Moreover, there was a positive correlation across clusters between the abundance of a cluster and its average Cx3cr1 transcript expression level in RFP regions, but not in YFP or mixed regions (Fig. S5 C). We thus hypothesized that CX3CL1, produced at higher levels by CIT9-RFP tumor cells, was a mediator of the suppressive TME in RFP regions of mixed tumors.

To functionally test the ability of tumor cell-produced CX3CL1 to drive an immunosuppressive microenvironment, we generated a CIT6-YFP cell line overexpressing Cx3cl1 (Cx3cl1-OE). We found CIT6-YFP^{Cx3cl1-OE} tumors grew more rapidly than CIT6-YFP-empty vector controls (Fig. 7 B). CIT6-YFP^{Cx3cl1-OE} tumors had an increased abundance of total macrophages compared with CIT6-YFP^{Empty} controls (Fig. 7 C), and strikingly, we found that this was driven specifically by an increase in $\text{CD206}^{\text{H{\sc i}}}$ macrophages in CIT6-YFP^{Cx3cl1-OE} tumors, while Arg1^{Hi} and MHC-IIHi macrophages showed no difference in frequency (Fig. 7 D). In line with this, expression of CX3CR1 was the highest on macrophages among all immune cell types (Fig. S5 D) and higher on CD206Hi macrophages compared with ArglHi and MHC-IIHi macrophages (Fig. 7 E). Additionally, we observed a lower abundance of neutrophils (Ly6G+) and monocytes (Ly6C+) in Cx3cl1-overexpressing CIT6-YFP tumors (Fig. 7 F). Other immune cell types, including B cells, CD8 T cells, and DCs, showed no difference in frequency (Fig. S5 E), however we observed higher frequency of CD4 T cells expressing exhaustion markers Tim3 and TIGIT (Fig. S5 F). We further asked whether exposure to supernatant from CIT6-YFPCx3cll-OE tumor cells,

compared with CIT6-YFP^{Empty} tumor cells, affected the suppressive capacity of macrophages. In a T cell suppression assay, we observed that bone marrow–derived macrophages pretreated for 48 h with CIT6-YFP^{Cx3cll-OE} supernatant showed an increased ability to suppress both CD4 and CD8 T cells, compared with those pre-treated with CIT6-YFP^{Empty} supernatant (Fig. 7 G).

To complement these overexpression experiments, we also carried out CRISPR-Cas9-mediated knock-out (KO) of Cx3cl1 in CIT9-RFP tumor cells and in uncolored CIT9 tumor cells, using distinct guide RNAs for each. We confirmed deletion of Cx3cl1 in single-cell clones by PCR and loss of CX3CL1 protein secretion in these clones by ELISA (Fig. S5 G). Cx3cl1-KO tumors showed a dramatic reduction in growth compared with controls (Fig. 7 H and Fig. S5 H) and a decreased level of CX3CL1 in tumor lysates as measured by ELISA (Fig. 7 I and Fig. S5 I), consistent with tumor cells themselves being an important source of CX3CL1 in the TME. CIT9-RFP^{Cx3cl1-KO} and CIT9^{Cx3cl1-KO} tumors further showed a decrease in total macrophage infiltrate (Fig. 7 J and Fig. S5 J). This was driven by a decrease in CD206Hi macrophages, while the abundance of Arg1Hi and MHC-IIHi macrophages remained similar between Cx3cl1-KO and control tumors (Fig. 7 K and Fig. S5 K). Of particular note, Cx3cl1-KO tumors showed a dramatic increase in T cell infiltrate (Fig. 7 L and Fig. S5 L), along with an increase in IFNγ⁺ CD8 T cells and Th1 cells, a decrease in Tregs, and a decrease in the ratio of Treg:Th1 and Treg:IFNγ+ CD8 T cells (Fig. 7, M and N), revealing that tumor cell-produced CX3CL1 is a significant mediator of the coldness of CIT9-RFP tumors.

Finally, since the combination of a CX3CL1^{High} and CX3CL1^{Low} tumor population was the product of mixing CIT9-RFP and CIT6-YFP tumor cells in our model system, we asked whether autochthonous DMBA/TPA-induced squamous skin carcinomas also exhibit spatial diversity in CX3CL1 and whether this associated with changes in the local immune microenvironment. Using 8 archival DMBA/TPA-induced skin carcinomas for which we had OCT blocks available (Reeves et al., 2018), we assessed CX3CL1 levels by IF staining. We determined that three of the eight tumors examined (38%) exhibited both high and low regions of CX3CL1 in the sections examined (Fig. 8 A). The remaining five tumors exhibited uniform low levels of CX3CL1 (data not shown). For the three tumors in which CX3CL1 exhibited variable spatial expression, we predicted macrophages would exhibit increased abundance in the vicinity of the



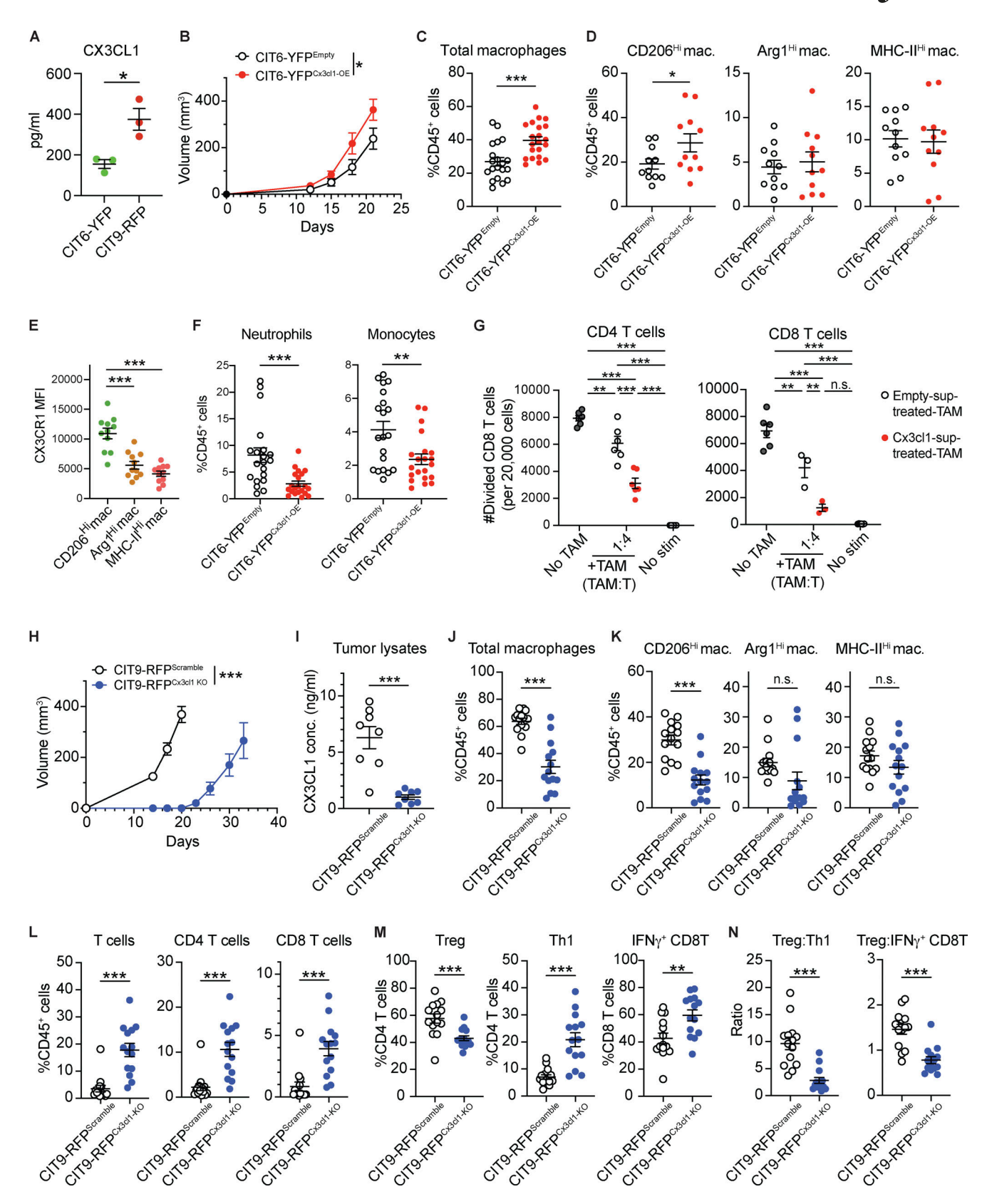


Figure 7. Chemokine Cx3cl1 mediates the CIT9-RFP-driven immunosuppressive TME. (A) ELISA-based quantification of CX3CL1 using tumor lysates of CIT6-YFP and CIT9-RFP single-population tumors (n = 3). (B) Tumor growth curves of CIT6-YFP tumors overexpressing CX3CL1 (CIT6-YFP^{Cx3cl1}) and empty vector (CIT6-YFP^{Empty}). n = 9-10. (C and D) Infiltration of total macrophages (C; n = 20-21) and macrophage subsets (D; n = 11) in CIT6-YFP^{Empty} and CIT6-YFP^{Cx3cl1} tumors. (E) Expression of CX3CR1 on macrophage subsets in CIT6-YFP^{Cx3cl1} tumors, measured as MFI from flow cytometric analysis. n = 11. (F) Frequency of neutrophils and monocytes in CIT6-YFP^{Cx3cl1} tumors (n = 20-21). Data in C-F are a representations or combinations of two independent



experiments. **(G)** CD4 and CD8 T cell suppression assay using bone marrow-derived monocytes treated with supernatants of CIT6-YFP^{Empty} or CIT6-YFP^{Cx3c11} cell lines (n = 3-6). Representation of three independent experiments. **(H)** Tumor growth curves of CIT9-RFP tumors deficient in CX3CL1 (Cx3c11 KO) and controls (scramble). n = 14-16. **(I)** Quantification of CX3CL1 using tumor lysates of CIT9-RFP scramble and Cx3c11 KO tumors (n = 8). **(J-M)** Frequency of total macrophages (J), macrophage subsets (K), T cells (L), and T cell subsets (M) infiltrating CIT9-RFP scramble and Cx3c11 KO tumors (n = 14). **(N)** Treg to Th1 and IFN γ ⁺ CD8 T cell ratios in CIT9-RFP scramble and Cx3c11 KO tumors (n = 14). Experiments for H–N were performed once. Statistical significance was determined by Student's t test (A, C, D, and I–N), one-way ANOVA (E), and two-way ANOVA with Tukey's correction posttest (B and G). *P < 0.05, **P < 0.01, and ***P < 0.001. MFI, median fluorescence intensity.

CX3CL1^{High} regions, and we co-stained these tumors for CX3CL1 and F4/80. Each tumor was divided into tiles, mean CX3CL1 expression, and number of F4/80⁺ cells (macrophages) quantified in each tile, and tiles divided by CX3CL1 intensity into top 50% (CX3CL1^{High}) and bottom 50% (CX3CL1^{Low}) regions. We observed that in all three tumors macrophages were significantly more abundant in Cx3cl1^{High} regions (Fig. 8, B and C), demonstrating that regions of high tumor-produced CX3CL1 are pockets of enriched macrophage accumulation in autochthonous tumors.

CX3CL1 is a mediator of a cold TME in human cancers

To assess the role of CX3CL1 in shaping the TME and myeloid cell abundance in human cancers, we turned to a previously published pan-cancer human dataset containing transcriptomic profiles of whole tumors and of individual immune compartments (e.g., myeloid compartment) from 364 individual tumors across 12 cancer types (Combes et al., 2022). Previous analysis identified 12 recurrent immune infiltration patterns across these 364 tumors, denoted "immune archetypes," spanning a range from immune-rich to immune-poor TMEs. Looking at T cell abundance, seven of these archetypes could be classified as immune hot and five of them as immune cold, corresponding with high and low T cell infiltrates based on T cell transcriptomic scores (Fig. 8 D). We assessed whole-tumor CX3CL1 RNA expression in each archetype and found that, strikingly, CX3CL1 levels were highest in three of five cold archetypes (archetypes 9, 10, and 12) and comparatively low in all hot archetypes (Fig. 8 E). Next, we examined the macrophage:monocyte ratio across all human archetypes, using transcriptomic scores for macrophages and monocytes based on RNA-seq data from the myeloid compartment of each tumor (Combes et al., 2022). We observed a bias in the myeloid compartment toward macrophages (log₂ of the macrophage:monocyte ratio >0) in the same three cold human archetypes that showed high CX3CL1 (archetypes 9, 10, and 12, Fig. 8 F). Using a gene signature based on the macrophage-3 cluster with the highest CD206 levels in our ZipSeq dataset, we also asked if CD206Hi macrophages were enriched in CX3CLIhigh human immune archetypes. We found that, among cold archetypes, the macrophage compartment showed a high CD206^{Hi} macrophage score in two archetypes, both of which were CX3CL1-high (archetypes 10 and 12, Fig. 8 G). Finally, we turned back to our Cx3cl1-overexpressing mouse tumors. We saw that CX3CL1 overexpression led to an increase in both the macrophage:monocyte ratio and the CD206hi macrophage:non-CD206hi macrophage ratio in Cx3cl1-overexpressing CIT6-YFP tumors compared with controls (Fig. 8 H). Of note, we also analyzed the seven hot human archetypes that show low CX3CL1 expression and found a range of macrophage:monocyte ratios

and CD206^{Hi} macrophage scores (Fig. S5 M), suggesting that additional and likely different factors shape these ratios in hot, CX3CL1-low tumors. Collectively, these data show that CX3CL1 is associated with cold TMEs enriched in CD206^{Hi} macrophages not only in our mouse model but also across multiple human cancers

Discussion

Combining fluorescently tagged hot and cold squamous cell skin carcinoma tumor populations, we have developed a novel model system to interrogate the spatial heterogeneity of tumor cells and intratumoral immune cells. When combined in a 1:1, 3:1, or 9:1 hot:cold tumor cell ratio, we see that an cold tumor population has a "dominant negative" effect. These findings are consistent with a previous report on a model of pancreatic cancer (Li et al., 2018); however, we have extended our model here to show that the cold tumor population can exert a suppressive effect even when it represents a minor population in the tumor. The overall immune phenotype of mixed-population tumors most closely resembles that of cold, immunosuppressive tumors, and these tumors exhibit a poor infiltration of CD8 T cells—which are critical to anti-tumor immunity—in all regions.

However, when we look at regions locally dominated by hot tumor cells (YFP+ regions in our tumors) or cold tumor cells (RFP+ regions in our tumors), we find that intratumoral immune activity is far from spatially uniform; but rather, is profoundly influenced by local tumor cells. CD4 T cells accumulate specifically in regions occupied by hot tumor cells, as do inflammatory monocytes and neutrophils. Both CD4 and CD8 T cells also show better effector phenotypes in the vicinity of hot tumor cells. By contrast, CD206Hi immunosuppressive macrophages preferentially accumulate in the neighborhoods of cold tumor cells, recruited by tumor-produced CX3CL1. Thus, although the immune response to the tumor as a whole is subject to host-wide factors, within the tumor, tumor cells themselves also set up a blueprint for the spatial architecture of infiltrating immune cells, with different tumor cell populations shaping distinct "micromicroenvironments" in their vicinities. Our study is the first, to our knowledge, to demonstrate a clear, reproducible link between spatial organization of infiltrating immune cells and the underlying spatial organization of tumor cells. This study did not address the question as to whether immune pressure conversely also influences the spatial arrangement of tumor subpopulations, but this is an interesting question for future work.

Tumor cell-driven spatial differences in the intratumoral immune response exist at baseline in the absence of therapy but also persist during immunotherapy and exert an influence on the response to therapy. Regional analysis of response to



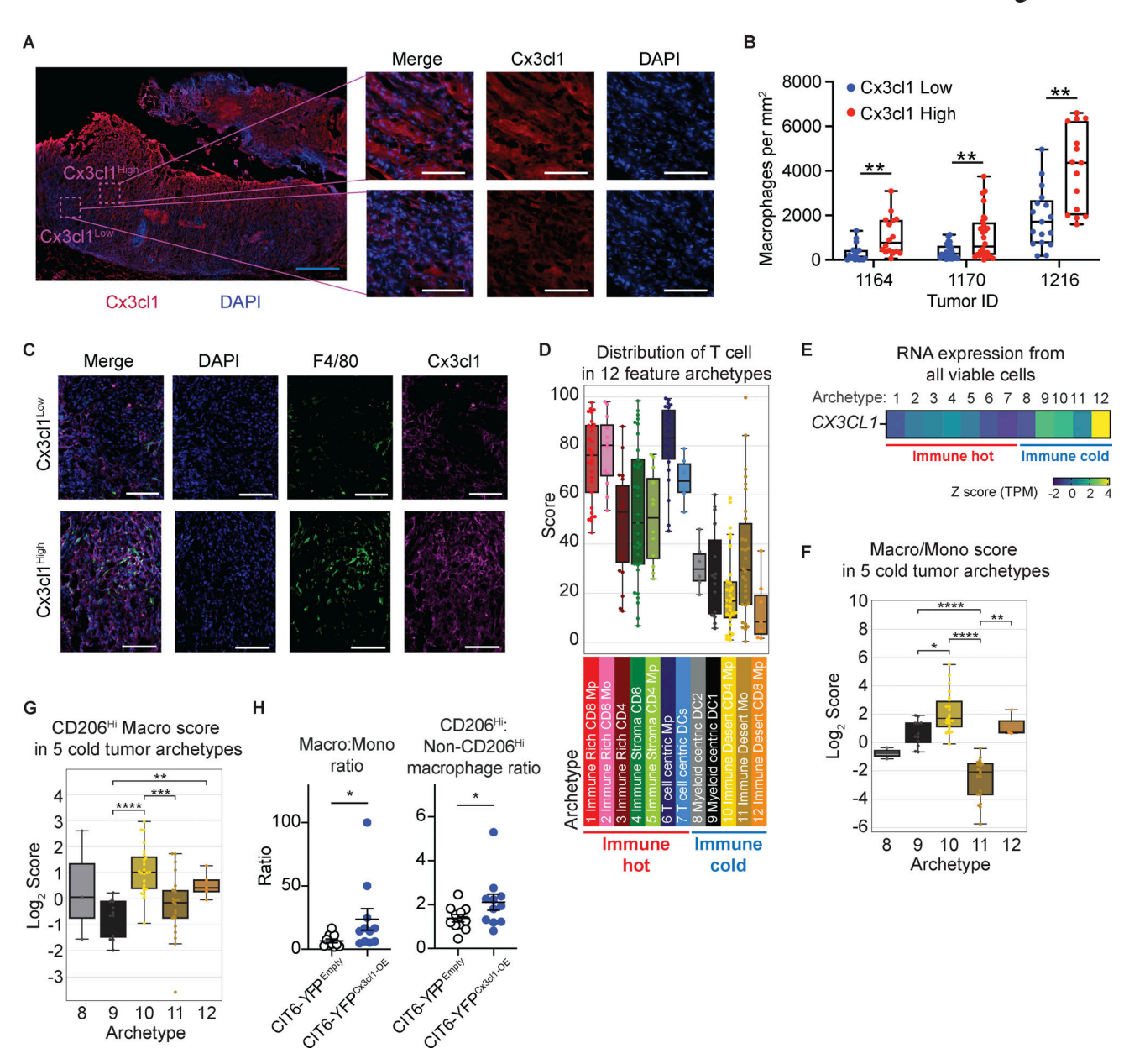


Figure 8. **CX3CL1 is a mediator of a cold TME in human cancers. (A)** Representative immunofluorescence staining of CX3CL1 in an autochthonous DMBA/TPA skin carcinoma, showing distinct regions of high and low CX3CL1. Blue scale bar = $500 \, \mu m$, white scale bar = $100 \, \mu m$. Representation of three tumors. **(B)** Quantification of F4/80* macrophages per mm² in CX3CL1 high and low regions of autochthonous DMBA/TPA skin carcinomas (n = 3 tumors, 15-28 tiles counted for each region). **(C)** Representative immunofluorescence staining of F4/80 in regions of low (top) and high (bottom) CX3CL1. Scale bar = $100 \, \mu m$. Representation of three tumors. **(D-G)** Analysis of immune cells and CX3CL1 expression using a previously published dataset of 364 human tumors from 12 cancer types. Computational clustering of tumors using flow cytometry data and transcriptomic data enabled identification of 12 dominant patterns of immune composition across various cancers, referred to as immune archetypes (Combes et al., 2022). RNA-seq data were generated separately for all viable cells and for sorted mononuclear phagocytes. Prior to RNA-seq, cells were sorted by flow cytometry from untreated, freshly resected human tumors. **(D)** T cell score of each tumor, based on RNA-seq of all viable cells, grouped on the x axis by immune archetype (n = 5-24). **(E)** Heatmap of average CX3CL1 RNA expression, based on RNA-seq of all viable cells, grouped on the x axis by immune archetype (n = 5-24). **(E)** Heatmap of average CX3CL1 RNA expression, based on RNA-seq of unimume archetypes (n = 5-24). **(F)** Ratio of macrophage score and monocyte score, based on RNA-seq of mononuclear phagocytes, for tumors in the five immune cold archetypes (n = 5-24). **(H)** Ratio of macrophages to monocytes (left) and CD206^{Hi} macrophages to non-CD206^{Hi} macrophages to non-CD206

anti-PD-1 blockade + anti-CD40 agonist combination immunotherapy showed that cold regions remained more poorly infiltrated by functional T cells than hot regions, indicating that therapy did not overcome the spatial patterning that existed pretreatment. While the anti-PD-1 plus CD40 agonist combination we employed failed to cure our mixed tumors, our model system facilitated detailed region-by-region analysis of the effects and efficacy of therapy. This system thus establishes a platform on



which additional drug combinations or dose regimens can be probed to iterate on how best to induce a productive tumor-wide anti-tumor immune response across all tumor regions. We note that the CIT6 and CIT9 tumor cell lines harbor 256 and 102 nonsynonymous mutations, respectively, but share only a single mutation, an Hras Q61L-driver mutation, between them. The mixed-population tumors thus represent tumors with few to no clonal antigens. As clonal antigens have been shown to be important in mediating tumor responses to immune checkpoint inhibitors (McGranahan et al., 2016; Nguyen et al., 2023; Westcott et al., 2023), it is possible the lack of clonal antigens also contributed to the failure of the anti-PD-1 plus CD40 agonist treatment. Recent literature has also highlighted that, in the context of multiple tumor antigens, an immunodominant antigen can negatively impact the response to other tumor antigens (Memarnejadian et al., 2017; Friedman et al., 2020; Burger et al., 2021). However, because we observed a consistently poor T cell response to CIT9 tumor cells even in homogeneous CIT9 tumors, we were unable to discern whether or not the presence of CIT6 antigens in mixed tumors was exerting a dynamic of immunodominance over CIT9 antigens. We acknowledge that the model system we employed, in which tumors were comprised of only two populations, does not represent the full spectrum of heterogeneity found in patient tumors. Pan-cancer analyses of subclonal structures of human tumors have suggested that they contain on average 3-5 clones, with the median number of clones varying based on tumor type (Andor et al., 2016; Wolf et al., 2019). In future work, our model system is amenable to the incorporation of additional tumor populations, which might enable us to detangle additional implications of higher levels of heterogeneity on the immune microenvironment.

Finally, we identify CX3CL1 as a mediator of the dominant immunosuppressive microenvironment, suggesting thatalthough our tumors are both genetically and transcriptionally heterogeneous—transcriptional heterogeneity is a key mediator of the impaired immune response in our studies. We show that CX3CL1-expressing tumor cells drive enrichment of immunosuppressive CD206Hi macrophages and depletion of inflammatory monocytes and neutrophils. Further, in autochthonous DMBA/TPA tumors, we find CX3CL1 frequently exhibits a nonuniform spatial pattern, and macrophages preferentially accumulate in CX3CL1-high tumor regions. In a pan-cancer analysis of human patients, high levels of CX3CL1 are associated with three specific immune cold TME archetypes, all of which show macrophage-enriched myeloid compartments, and 2 of the 3 show a specific enrichment of $CD206^{Hi}$ macrophages. The CX3CR1:CX3CL1 axis has also been found to be linked to macrophage accumulation in both squamous cell skin carcinomas and breast tumors on a whole-tumor level (Reed et al., 2012; Ishida et al., 2020). Further, our findings that CX3CL1 is a candidate mediator of local immunosuppressive myeloid cell organization are in line with previous reports of chemokine-driven spatial organization of immune cells within tumors (Pelka et al., 2021; Miheecheva et al., 2022). Of note, CX3CL1 has also been described as an "anti-tumor" chemokine, particularly in lung cancer, due to its role interacting with CX3CR1+ T cells (Kee et al., 2013; Gerlach et al., 2016; Liu et al., 2019b; Korbecki

et al., 2020), highlighting that its role in tumor immunity is context-dependent and not yet fully understood. Careful investigation will be essential to assess the therapeutic potential of CX3CL1 blockade as a strategy to improve immunotherapy responses in cold tumors. Of course, CX3CL1 does not fully define the immune microenvironment. Future work, in addition to more deeply investigating the role of CX3CL1, is also expected to uncover additional pathways by which tumor cells shape their local micro-microenvironments and influence responses to immunotherapy on a highly local spatial scale.

Materials and methods

Carcinogenesis and cell line generation

To induce tumors, K5-CreER^{T2}-Confetti FVB/N mice were treated with 25 μ g DMBA followed by TPA (200 μ l of a 10⁻⁴ M solution in acetone) two times a week for 20 wk, as described (Reeves et al., 2018). To generate cell lines, carcinomas were resected at a size of >1 cm in longest diameter, finely chopped, digested in DMEM containing Collagenase I and IV and DNase I for 45 min at 37°C, washed with PBS, plated in supplemented DMEM (high-glucose DMEM [catalog# 11995065; Gibco] plus 10% heatinactivated FBS [Gibco], 2 mM L-glutamine, with 100 U/ml penicillin, 100 μ g/ml streptomycin, and 2.5 μ g/ml amphotericin B [Gibco]), and passaged until cells stably grow in culture. The established cell lines were cultured in the supplemented DMEM for all experiments.

Cell line sequencing

DNA was extracted from cultured cells from each cell line and from tails of the mice in which each tumor originated using the Qiagen DNeasy Blood & Tissue DNA purification kit (Qiagen). Whole-exome sequencing was performed using the Agilent Sure Select Mouse Exon capture kit and sequenced to an average depth of 153X on an Illumina HiSeq X by MedGenome, Inc. Reads were trimmed with cutadapt (v3.5) (Martin, 2011) and aligned to the mm10 mouse genome using BWA (v0.7.17) (Li and Durbin, 2009). Reads were deduplicated with MarkDuplicates and recalibrated with BaseRecalibrator from GATK (v4.1) (Van der Auwera and O'Connor, 2020). Mutations were called using MuTect2 (GATK v4.1) (Cibulskis et al., 2013; Van der Auwera and O'Connor, 2020) and Strelka2 (v2.9.10) (Kim et al., 2018), using tails from the mice in which each tumor developed as the matched normal. Mutation calls were filtered using the following criteria: minimum read depth of 10 at the mutation position in both tumor and normal samples; minimum of for reads supporting the mutation call; for Strelka only, minimum quality score (QSS) of 25. Mutations that passed all filters with both callers were kept and were additionally filtered to remove any germline SNP detected in the panel of normals. Final mutation calls were annotated with Annovar (Wang et al., 2010). Exome sequencing data from CIT lines are available in SRA accession number PRJNA1129114.

Cell line labeling

Unlabeled cell lines were treated with adenoviral Cre recombinase (catalog #1045; Vector Biolabs) to induce labeling



with Confetti fluorescent proteins. YFP- and RFP-expressing cells were sorted via fluorescence-activated cell sorter and further grown in vitro to establish CIT6-YFP and CIT9-RFP cell lines.

In vivo experiments

A total of 1.25×10^5 cells were injected subcutaneously into the dorsal flank of 8-16-wk-old male and female Confettihomozygous FVB/N mice. Approximately 21-28 days later, when tumors measured ~1 cm in diameter, tumors were dissected and digested as described above and subsequently used in flow cytometric analysis. For treatment experiments, when tumors measured ~5 mm in diameter, mice were injected intraperitoneally with one dose (CD40 agonistic antibody) or two doses (anti-PD-1 antibody) of therapeutic antibodies, administered at a 3-day interval. Antibodies used were rat anti-mouse PD-1 IgG2a antibody (RMP1-14; BioXCell), rat anti-CD40 agonist IgG2a antibody (FGK4.5; BioXCell), and rat IgG2a isotype control (2A3; BioXCell) at 200 µg per antibody per dose. Tumors were resected at 1 cm in diameter and used for downstream analyses, except in 6-day after treatment analyses, where tumors were resected 6 days after treatment initiation. All animal experiments were approved by the University of California, San Francisco Laboratory Animal Resource Center (#AN187679; Institutional Animal Care and Use Committee [IACUC]) or by the University of Utah Office of Comparative Medicine (#22-02003; IACUC). This work complies with all the relevant ethical regulations regarding animal research.

Flow cytometric immune profiling and macrophage cell sorting

For whole tumor analysis and sorting, 5 million cells were stained with antibodies. For spatial immune profiling, tumors were embedded in 2% agarose gel, sliced into 400-µm sections by a Leica Vibratome, and microdissected into YFP, RFP, and mixed regions using a surgical scalpel while visualizing each region on an MVX10 fluorescent stereoscope. Multiple pieces of each region from a single tumor were pooled for digestion, followed by flow cytometric analysis. Cell sorting was performed on FACS Aria III (BD Biosciences). Antibodies used for flow cytometric analyses and sorting are listed in Table 1.

Immunofluorescence imaging

After half of the tumors were processed for flow cytometric analysis, the remaining halves were fixed in 4% paraformaldehyde for 2 h, dehydrated in PBS with 30% sucrose overnight at 4°C, embedded in Tissue-tek O.C.T. compound (Sakura Finetek USA), and stored at -80°C. Embedded blocks were cryosectioned into 8-µm sections using a Leica CM3050 S Cryostat (Leica Biosystems). Sections were stained with primary antibody overnight (CD3: #ab5690; Abcam; CD45: #14-0451-85; Invitrogen; CX3CL1: #MAB571; R&D systems [rat] and #NBP1-49539; Novus [rabbit]; and F4/80: #70076; Cell Signaling Technology), followed by staining with secondary antibody for 1 h (anti-rabbit Alexa Fluor 647 [#A-21245; Invitrogen]; anti-rat Alexa Fluor

Table 1. Antibodies used for flow cytometry

Marker	Fluorophore	Clone	Manufacturer
CD45	AlexaFluor700	30-F11	BioLegend
CD45	VF500	30-F11	Tonbo Biosciences
F4/80	BV421	BM8	BioLegend
F4/80	APC	BM8	BioLegend
F4/80	RedFluor710	BM8.1	Tonbo Biosciences
CD11c	BV605	N418	BioLegend
Ly6C	BV650	HK1.4	BioLegend
CD11b	BV711	M1/70	BioLegend
CD8a	BV785	53-6.7	BioLegend
CD8a	PE-Cy7	2.43	Tonbo Biosciences
CD3e	BUV395	145-2C11	BD Biosciences
CD4	BUV563	GK1.5	BD Biosciences
B220	BUV661	RA3-6B2	BD Biosciences
Ly6G	PE-CF594	1A8	BD Biosciences
MHC-II	PE-Cy7	M5/114.15.2	BioLegend
MHC-II	FITC	M5/114.15.2	BioLegend
CX3CR1	APC	SA011F11	BioLegend
CX3CR1	PE	SA011F11	BioLegend
CX3CR1	BV421	28-50	BD Biosciences
Arg1	eFluor450	A1exF5	Invitrogen
CD206	BV785	C068C2	BioLegend
CD206	PE	C068C2	BioLegend
TNFα	PerCPCy5.5	MP6-XT22	BioLegend
Foxp3	APC	FJK-16s	Invitrogen
CD25	BV421	PC61	BioLegend
CD25	eFluor450	PC61.5	Invitrogen
PD-1	BV605	29F.1A12	BioLegend
Tim-3	APC	RMT3-23	BioLegend
TIGIT	BV421	1G9	BioLegend
IL17A	BV650	TC11-18H10.1	BioLegend
IL-4	BV786	11B11	BD Biosciences
ΙΕΝγ	BUV737	XMG1.2	BioLegend
CD39	PE-Dazzle594	Duha59	BioLegend
CD69	BV605	H1.2F3	BioLegend
CD44	BV785	IM7	BioLegend
CD62L	BUV737	MEL-14	BD Biosciences
NKp46	BV421	29A1.4	BioLegend
MHC-I (H-2Kq)	BV421	KH114	BD Biosciences
MHC-I (H-2Dq, Lq)	Biotin	KH117	BD Biosciences
CD16/32	N/A	2.4G2	Tonbo Biosciences
Live/dead	Fixable near-IR	N/A	Invitrogen

Antibodies used for flow cytometry listed by marker, fluorophore, clone, and manufacturer.



647 [#A-21247; Invitrogen]; anti-rat Alexa Fluor 594 [#A-48264; Invitrogen]; or anti-rabbit Alexa Fluor 488 [#A-11034; Invitrogen]) and DAPI stained for 5 min. Fluorescence images were taken on a DMi8 microscope (Leica Biosystems) using Leica Application Suite X (Leica Biosystems) imaging software or on a Nikon Eclipse Ti2 microscope (Nikon Metrology Inc.) using NIS-Elements AR ver 5.41.02 (Nikon Metrology Inc.) imaging software. Fraction of YFP+ and RFP+ cells as well as the number of CD3+ cells in each tile were quantified using Cell-Profiler ver. 3.1.9. CD45+ cells in CIT6-YFP and CIT9-RFP tumors, and Cx3cl1 expression and F4/80⁺ cells in autochthonous DMBA/ TPA tumors were quantified using QuPath ver 0.5.1. CD45+ cells in CIT6-YFP and CIT9-RFP tumors were quantified using QuPath ver 0.5.1. Total cells in each image were quantified based on DAPI stain using QuPath's Cell Detection method. CD45+ cells were identified using QuPath's Pixel Classifier method to assign each detected cell as CD45+ or CD45-.

Overexpression of cytokines and chemokines

Mouse *Cx3cl1* gene was amplified using the forward primer 5′-AACTCGAGATGGCTCCCTCGCCGCTCG-3′ and reverse primer 5′-TTCCGCGGTCACACTGGCACCAGGACGTA-3′, cDNAs generated from CIT9 cell line and Q5 High-Fidelity DNA polymerase (NEB). MSCV 2.2-IRES-CFP retroviral vector was generated by replacing GFP of MSCV 2.2-IRES-GFP vector (obtained from James Carlyle lab at the University of Toronto, Toronto, Canada) with CFP. Using restriction enzymes XhoI and SacII, *Cx3cl1* coding sequencing was cloned into the MSCV 2.2-IRES-GFP vector. Proviral vectors Gag/Pol and VSV-G were co-transfected with Cx3cl1-IRES-GFP MSCV2.2 vector using lipofectamine 3000 (Invitrogen) into HEK293T cells. 48 h later, the viruses were collected, mixed with CIT6-YFP cells, and spinfected at 800 *g* for 90 min. YFP+ CFP+transduced cells were sorted 72 h after transduction.

Generation of Cx3cl1 KO cell lines

To generate CIT9-RFP Cx3cl1 KO cell line, equal mixture of 160 µM trans-activating CRISPR RNA (tracrRNA) and 10 nmol CRISPR RNA (crRNA), the latter of which was resuspended in duplex buffer, was incubated for 30 min at 37°C. Two crRNA combinations were used; 5'-TCAGTCCAAAACAACCCCAG-3' (protospacer-adjacent motif [PAM] AGG) and 5'-TCAGCGAGG AGATAGCCTGT-3' (PAM GGG) targeting exon 2 of Cx3cl1, and negative control (Scrambled) crRNA sequence was 5'-GGTTCT TGACTACCGTAATT-3'. Equal amount of 40 µM Cas9 protein and tracrRNA:crRNA complex was incubated for an additional 15 min at 37°C. 2×10^5 CIT9-RFP cells resuspend in 20 μl of supplemented SG buffer were mixed with the RNP complex and 100 µM single-stranded DNA (ssDNA) non-targeting electroporation stabilizer (5'-GCCACCTACGGCAAGCTGACCCTGAAG TTCATCTGCACCACCGGCAAGCTGCCCGTGCCCTGGCCCACC CTCGTGACCACCCTGACGTACGGCGTGCAGTGCTTCAGCCGC TACCCCGACCACATGA-3') and electroporated in 16-well Nucleocuvette Strips using Lonza 4D-Nucleofector X unit and program EN-158. The cells and supernatant were collected, single clones were expanded and analyzed for KO by PCR (primers; 5'-GAGCTCAAAGCCAGTCTGATTGTC-3' and 5'-TCTGGA TCCTGCTCTAGTAGGCCA-3') and ELISA 4-5 days after

transfection. To generate CIT9 Cx3cl1 KO cell line, 18.5 pmol of Cas9 protein and 180 pmol of guide RNAs (gRNA-1, 5'-CCTCCC ACCGCCTCCTACTG-3', and gRNA-2, 5'-AGTACACAAATGGAA GAACG-3') targeting exon1 of Cx3cl1, were combined and mixed gently with SF Cell Line Nucleofector Solution. The mixture was then incubated at 37°C for 20 min to allow for RNP formation. 200k CIT9-PAR cells were then resuspended in 20 μ l of SF nucleofector solution, and 10 µl of the RNP complex was added and mixed with the suspended cells. Nucleofection mixes were added to Nucleocuvette Strips and electroporated using a Lonza 4D-Nucleofector X unit in the program DS-138. The electroporated cells were transferred to 12-well plates to grow for 48-72 h. Consequently, cells were stained with an anti-mouse CX3CL1/ Fractalkine APC-conjugated antibody. Unstained single cells were sorted using an Aria Cell Sorter and grown to form singlecell colonies. Colonies derived from single-sorted Cx3cl1-/- cells were further screened by PCR using primers 5'-GCATCGCAT GGGCGAAAG-3' and 5'-GAGTCGGGGAGACACCTCG-3'. Cell supernatants were screened using ELISA.

ZipSeq spatial transcriptomics analysis

Mixed-population tumors were harvested at 1 cm in diameter and sliced into 200- μ m sections in 2% agarose using vibratome. Sections selected to be analyzed were incubated with a CD45 antibody linked to Cy5-conjugated photocaged oligo for 1 h at 4C°, followed by patterned illumination of a user-defined region of interest (Hu et al., 2020) and incubation with a unique zipcode. The process was repeated for YFP, RFP, and mixed regions. Sections were then digested in a collagenase I and IV blend for 30 min at room temperature and sorted for live Cy5+ cells using FACS Aria II, washed in PBS + 0.04% BSA, and then encapsulated following 10× Genomics specifications for 3' v3 chemistry with a target cell number of 8,000.

Libraries were sequenced with a target number of 30,000 reads per cell for gene expression and 3,000 reads per cell for zipcode barcodes on an Illumina NovaSeq. Demultiplexed fastqs were aligned using CellRanger to the mm10 Ensembl 93 reference genome. Count matrices were used to generate Seurat objects in R, keeping only cells with at least 200 detected genes and genes found in at least three cells. Cells were further filtered based on a minimum 500 gene cutoff and a maximum 15% mitochondrial reads. Zipcode counts were normalized using a centered log ratio transform and then assigned a dominant zipcode identity (as in Hu et al. [2020]). Cells were then passed through SCTransform regressing for percent mitochondrial reads. Following principal component analysis on the top variable genes, the first 18 principal components were used as inputs for UMAP dimensional reduction and clustering via the FindNeighbors and FindClusters commands. For pathway analysis, lists of genes with average log₂ fold change >1 for each cluster were used as input for the GO Biological Process 2021 repository on EnrichR (Xie et al., 2021). scRNA-seq data generated in the ZipSeq experiments are available in GEO accession number GSE237233.

Cytokine array

70-150 mg of tumor pieces were chopped into small pieces in radioimmunoprecipitation assay buffer containing proteinase



inhibitor (Cell BioLabs) and homogenized using OctoMACS (Miltenyi Biotec). The homogenate was centrifuged at 400 g for 5 min, followed by further centrifugation at 10,000 g for 10 min at 4°C. The supernatant was collected and stored at -80° C. Protein concentration was measured using DC protein assay kit (BioRad). The sample concentrations were normalized prior to the submission for the analysis by Eve Technologies DM-44 mouse Discovery Assay panel.

In vitro T cell suppression co-culture assay

CD8 T cells were isolated from the lymph node or spleen of naïve mice using EasySep Mouse CD8+ T cell Isolation Kit, Mouse Naïve CD8+ T cell Isolation Kit or Mouse Naïve CD4+ T cell Isolation Kit (StemCell Technologies). Macrophages were sorted from the tumors via FACS sorting. CD8 T cells were labeled with CFSE and co-cultured with the macrophages at varying ratios in the presence of Mouse T-Activator CD3/CD28 Dynabeads (Gibco) and analyzed for division and T cell activation markers. For T cell suppression co-culture assay with cell line supernatant-treated macrophages, bone marrow-derived monocytes isolated from naïve mice were differentiated into macrophages for 5 days in 50 µg/ml M-CSF. Macrophages were then treated with supernatant of CIT6-YFP^{Empty} and CIT6-YFP^{Cx3xl1-OE} cells lines for 2 days (day 6-7) before co-culture, beginning on day 8, with CD4 or CD8 T cells stimulated with CD3/28 Dynabeads.

Immune cell abundance analysis for human RNA-seq dataset

For analysis of human tumors, T cell, macrophage, and monocyte scores were based on previously calculated scores using an average expression level of genes that are uniquely expressed in human T cells, macrophages, and monocytes (Combes et al., 2022). The CD206^{Hi} macrophage score was calculated by identifying a combination of four genes that are uniquely expressed in the macrophage-3 cluster (cluster 4) of our ZipSeq dataset from the first tumor analyzed (*Hmoxl*, *Cx3cr1*, *Folr2*, and *Fl3al*). This score was normalized against the average expression level of four genes (*Ccr2*, *Mgl2*, *Nr4a2*, and *Ciita*), which were expressed in other macrophages but were not expressed in the cluster 4.

Statistical analysis

Data distribution was assumed to be normal, but this was not formally tested. Data were analyzed using Prism 9 (GraphPad) with either Student's t test for experiments with two arms, oneway ANOVA analysis for experiments with one variable and more than three experiment conditions, or two-way ANOVA for experiments with two variables and more than three experiment conditions. Bonferroni correction was used as a posttest of ANOVA. For Kaplan–Meier survival analyses, the log-rank test was used. Graphs show mean \pm SEM or mean \pm SD.

Online supplemental material

Fig. S1 shows the abundance of additional immune cell subsets in CIT6-YFP and CIT9-RFP tumors, flow cytometric gating strategy used for immune cell analysis, and data on establishment of mixed tumors. Fig. S2 contains the functional analysis of tumor-

infiltrating macrophages, analysis of immune cell abundance in mixed tumors, and quantification of immune cells in tumors following PD-1 blockade + CD40 agonist combination immunotherapy. Fig. S3 contains the additional analysis of ZipSeq data from the tumor shown in Fig. 6, as well as ZipSeq analysis of a second mixed-population tumor. Fig. S4 shows the additional analysis of macrophage subsets in mixed tumors and results of full cytokine and chemokine array on CIT6-YFP and CIT9-RFP tumors. Fig. S5 contains the analysis of Cx3crl in the ZipSeq datasets and by flow cytometry, data on immune cell infiltration in CIT6-YFP^{Cx3cll-OE} and CIT9-RFP^{Cx3cll-KO} tumors, and data on macrophage scores by immune archetype for immune hot archetypes.

Data availability

The data that support the findings in this study are available from the corresponding author upon request. scRNA-seq data generated in the ZipSeq experiments are available in GEO (accession number GSE237233). Exome sequencing of CIT lines is available in SRA (accession number PRJNA1129114).

Acknowledgments

We thank the University of California, San Francisco (UCSF) Biological Imaging Development CoLab, UCSF Parnassus Flow CoLab RRID:SCR_018206, the University of Utah Flow Cytometry Core, the University of Utah Center for High Performance Computing, and the University of Utah Mutation Generation and Detection Core Facility. We thank R. Judson-Torres and R. Belote for providing access to and assistance with the Nikon Ti2 Eclipse microscope, and all members of the Reeves Lab for thoughtful input during the development of this story.

This work was supported by the UCSF Program for Breakthrough Biomedical Research Sandler Fellowship, U.S. National Cancer Institute grant R21CA264599, the Huntsman Cancer Institute Cancer Center Support Grant P30CA040214, the Parker Institute for Cancer Immunotherapy, the American Cancer Society (IRG-21-131-01), Five For The Fight, The Cancer League, and the V Foundation (V2024-002). K.H. Hu is supported by the Cancer Prevention and Research Institute of Texas Scholar in Cancer Research award (RR230012), the University of Texas Rising STARS award, and the Parker Institute for Cancer Immunotherapy and V Foundation Bridge award. K. Kersten is supported by start-up funds from Sanford Burnham Prebys. The computational resources used were partially funded by the National Institutes of Health Shared Instrumentation Grant 1S10OD021644-01A1.

Author contributions: M. Tanaka: conceptualization, data curation, formal analysis, investigation, methodology, project administration, resources, validation, visualization, and writing—original draft, review, and editing. L. Lum: conceptualization, data curation, formal analysis, investigation, methodology, project administration, resources, software, validation, visualization, and writing—review and editing. K.H. Hu: formal analysis, investigation, methodology, and writing—review and editing. P. Chaudhary: conceptualization, investigation, methodology, validation, visualization, and writing—review and



editing. S. Hughes: investigation, validation, and writing review and editing. C. Ledezma-Soto: data curation, formal analysis, investigation, validation, and visualization. B. Samad: formal analysis. D. Superville: investigation. K. Ng: investigation. A. Chumber: formal analysis and investigation. C. Benson: investigation. Z.N. Adams: conceptualization, investigation, methodology, and writing—review and editing. K. Kersten: investigation. O.A. Aguilar: investigation, methodology, resources, supervision, and validation. L. Fong: conceptualization, data curation, formal analysis, funding acquisition, investigation, methodology, project administration, resources, supervision, visualization, and writing-review and editing. A.J. Combes: formal analysis, funding acquisition, investigation, resources, visualization, and writing—review and editing. M.F. Krummel: methodology. M.Q. Reeves: conceptualization, formal analysis, funding acquisition, investigation, methodology, project administration, resources, supervision, validation, and writingoriginal draft, review, and editing.

Disclosures: L. Fong reported personal fees from AbbVie, grants from BMS, personal fees from Dendreon, grants from Bavarian Nordic, grants from Merck, grants from Roche/Genentech, personal fees from Innovent, personal fees from Sutro, grants from Janssen, personal fees from Daiichi Sankyo, and personal fees from RAPT outside the submitted work; L. Fong also reported equity interest in Actym, Bioatla, Immunogenesis, Nutcracker, and Senti. A.J. Combes reported grants from Genentech Roche, grants from Eli Lilly, and personal fees from Foundery innovation outside the submitted work. No other disclosures were reported.

Submitted: 2 December 2024 Revised: 23 February 2025 Accepted: 25 February 2025

References

- AbdulJabbar, K., S.E.A. Raza, R. Rosenthal, M. Jamal-Hanjani, S. Veeriah, A. Akarca, T. Lund, D.A. Moore, R. Salgado, M. Al Bakir, et al. 2020. Geospatial immune variability illuminates differential evolution of lung adenocarcinoma. *Nat. Med.* 26:1054–1062. https://doi.org/10.1038/s41591-020-0900-x
- Andor, N., T.A. Graham, M. Jansen, L.C. Xia, C.A. Aktipis, C. Petritsch, H.P. Ji, and C.C. Maley. 2016. Pan-cancer analysis of the extent and consequences of intratumor heterogeneity. *Nat. Med.* 22:105–113. https://doi.org/10.1038/nm.3984
- Burger, M.L., A.M. Cruz, G.E. Crossland, G. Gaglia, C.C. Ritch, S.E. Blatt, A. Bhutkar, D. Canner, T. Kienka, S.Z. Tavana, et al. 2021. Antigen dominance hierarchies shape TCF1+ progenitor CD8 T cell phenotypes in tumors. Cell. 184:4996-5014.e26. https://doi.org/10.1016/j.cell.2021.08.020
- Chen, D.S., and I. Mellman. 2017. Elements of cancer immunity and the cancer-immune set point. *Nature*. 541:321–330. https://doi.org/10.1038/nature21349
- Cibulskis, K., M.S. Lawrence, S.L. Carter, A. Sivachenko, D. Jaffe, C. Sougnez, S. Gabriel, M. Meyerson, E.S. Lander, and G. Getz. 2013. Sensitive detection of somatic point mutations in impure and heterogeneous cancer samples. *Nat. Biotechnol.* 31:213–219. https://doi.org/10.1038/nbt.2514
- Combes, A.J., B. Samad, J. Tsui, N.W. Chew, P. Yan, G.C. Reeder, D. Kushnoor, A. Shen, B. Davidson, A.J. Barczak, et al. 2022. Discovering dominant tumor immune archetypes in a pan-cancer census. *Cell*. 185:184–203.e19. https://doi.org/10.1016/j.cell.2021.12.004

- Conroy, M.J., and J. Lysaght. 2020. CX3CL1 signaling in the tumor microenvironment. Adv. Exp. Med. Biol. 1231:1–12. https://doi.org/10.1007/978-3-030-36667-4-1
- Darvin, P., S.M. Toor, V. Sasidharan Nair, and E. Elkord. 2018. Immune checkpoint inhibitors: Recent progress and potential biomarkers. Exp. Mol. Med. 50:1–11. https://doi.org/10.1038/s12276-018-0191-1
- Das, S., and D.B. Johnson. 2019. Immune-related adverse events and antitumor efficacy of immune checkpoint inhibitors. J. Immunother. Cancer. 7:306. https://doi.org/10.1186/s40425-019-0805-8
- DeNardo, D.G., and B. Ruffell. 2019. Macrophages as regulators of tumour immunity and immunotherapy. Nat. Rev. Immunol. 19:369–382. https:// doi.org/10.1038/s41577-019-0127-6
- Friedman, J., E.C. Moore, P. Zolkind, Y. Robbins, P.E. Clavijo, L. Sun, S. Greene, M.V. Morisada, W.K. Mydlarz, N. Schmitt, et al. 2020. Neo-adjuvant PD-1 immune checkpoint blockade reverses functional immunodominance among tumor-antigen specific T cells. Clin. Cancer Res. 26:679-689. https://doi.org/10.1158/1078-0432.CCR-19-2209
- Galon, J., and D. Bruni. 2019. Approaches to treat immune hot, altered and cold tumours with combination immunotherapies. Nat. Rev. Drug Discov. 18:197–218. https://doi.org/10.1038/s41573-018-0007-y
- Gejman, R.S., A.Y. Chang, H.F. Jones, K. DiKun, A.A. Hakimi, A. Schietinger, and D.A. Scheinberg. 2018. Rejection of immunogenic tumor clones is limited by clonal fraction. *Elife*. 7:e41090. https://doi.org/10.7554/eLife 41090
- Gerlach, C., E.A. Moseman, S.M. Loughhead, D. Alvarez, A.J. Zwijnenburg, L. Waanders, R. Garg, J.C. de la Torre, and U.H. von Andrian. 2016. The chemokine receptor CX3CR1 defines three antigen-experienced CD8 T cell subsets with distinct roles in immune surveillance and homeostasis. *Immunity*. 45:1270–1284. https://doi.org/10.1016/j.immuni.2016
- Gerlinger, M., A.J. Rowan, S. Horswell, M. Math, J. Larkin, D. Endesfelder, E. Gronroos, P. Martinez, N. Matthews, A. Stewart, et al. 2012. Intratumor heterogeneity and branched evolution revealed by multiregion sequencing. N. Engl. J. Med. 366:883-892. https://doi.org/10.1056/NEJMoa1113205
- Hu, K.H., J.P. Eichorst, C.S. McGinnis, D.M. Patterson, E.D. Chow, K. Kersten, S.C. Jameson, Z.J. Gartner, A.A. Rao, and M.F. Krummel. 2020. ZipSeq: Barcoding for real-time mapping of single cell transcriptomes. *Nat. Methods*. 17:833–843. https://doi.org/10.1038/s41592-020-0880-2
- Hu, X., J. Fujimoto, L. Ying, J. Fukuoka, K. Ashizawa, W. Sun, A. Reuben, C.W. Chow, N. McGranahan, R. Chen, et al. 2019. Multi-region exome sequencing reveals genomic evolution from preneoplasia to lung adenocarcinoma. Nat. Commun. 10:2978. https://doi.org/10.1038/s41467-019-10877-8
- Ishida, Y., Y. Kuninaka, Y. Yamamoto, M. Nosaka, A. Kimura, F. Furukawa, N. Mukaida, and T. Kondo. 2020. Pivotal involvement of the CX3CL1-CX3CR1 axis for the recruitment of M2 tumor-associated macrophages in skin carcinogenesis. J. Invest. Dermatol. 140:1951-1961.e6. https://doi.org/10.1016/j.jid.2020.02.023
- Kee, J.-Y., Y. Arita, K. Shinohara, Y. Ohashi, H. Sakurai, I. Saiki, and K. Koizumi. 2013. Antitumor immune activity by chemokine CX3CL1 in an orthotopic implantation of lung cancer model in vivo. Mol. Clin. Oncol. 1: 35–40. https://doi.org/10.3892/mco.2012.30
- Kim, S., K. Scheffler, A.L. Halpern, M.A. Bekritsky, E. Noh, M. Källberg, X. Chen, Y. Kim, D. Beyter, P. Krusche, and C.T. Saunders. 2018. Strelka2: Fast and accurate calling of germline and somatic variants. *Nat. Methods*. 15:591–594. https://doi.org/10.1038/s41592-018-0051-x
- Korbecki, J., D. Simińska, K. Kojder, S. Grochans, I. Gutowska, D. Chlubek, and I. Baranowska-Bosiacka. 2020. Fractalkine/CX3CL1 in neoplastic processes. Int. J. Mol. Sci. 21:3723. https://doi.org/10.3390/ijms21103723
- Li, H., and R. Durbin. 2009. Fast and accurate short read alignment with Burrows-Wheeler transform. Bioinformatics. 25:1754–1760. https://doi.org/10.1093/bioinformatics/btp324
- Li, J., K.T. Byrne, F. Yan, T. Yamazoe, Z. Chen, T. Baslan, L.P. Richman, J.H. Lin, Y.H. Sun, A.J. Rech, et al. 2018. Tumor cell-Intrinsic factors underlie heterogeneity of immune cell infiltration and response to immunotherapy. *Immunity*. 49:178–193.e7. https://doi.org/10.1016/j.immuni.2018.06.006
- Liu, D., B. Schilling, D. Liu, A. Sucker, E. Livingstone, L. Jerby-Arnon, L. Zimmer, R. Gutzmer, I. Satzger, C. Loquai, et al. 2019a. Integrative molecular and clinical modeling of clinical outcomes to PDI blockade in patients with metastatic melanoma. *Nat. Med.* 25:1916–1927. https://doi.org/10.1038/s41591-019-0654-5
- Liu, J., Y. Li, X. Zhu, Q. Li, X. Liang, J. Xie, S. Hu, W. Peng, and C. Li. 2019b. Increased CX3CL1 mRNA expression level is a positive prognostic factor



- in patients with lung adenocarcinoma. Oncol. Lett. 17:4877–4890. https://doi.org/10.3892/ol.2019.10211
- Martin, M. 2011. Cutadapt removes adapter sequences from high-throughput sequencing reads. *EMBnet. J.* 17:10–12. https://doi.org/10.14806/ej.17.1
- McCreery, M.Q., K.D. Halliwill, D. Chin, R. Delrosario, G. Hirst, P. Vuong, K.-Y. Jen, J. Hewinson, D.J. Adams, and A. Balmain. 2015. Evolution of metastasis revealed by mutational landscapes of chemically induced skin cancers. *Nat. Med.* 21:1514–1520. https://doi.org/10.1038/nm.3979
- McGranahan, N., A.J.S. Furness, R. Rosenthal, S. Ramskov, R. Lyngaa, S.K. Saini, M. Jamal-Hanjani, G.A. Wilson, N.J. Birkbak, C.T. Hiley, et al. 2016. Clonal neoantigens elicit T cell immunoreactivity and sensitivity to immune checkpoint blockade. *Science*. 351:1463–1469. https://doi.org/10.1126/science.aaf1490
- McGranahan, N., and C. Swanton. 2017. Clonal heterogeneity and tumor evolution: Past, present, and the future. *Cell.* 168:613–628. https://doi.org/10.1016/j.cell.2017.01.018
- Mehta, A.K., S. Kadel, M.G. Townsend, M. Oliwa, and J.L. Guerriero. 2021.
 Macrophage biology and mechanisms of immune suppression in breast cancer. Front. Immunol. 12:643771. https://doi.org/10.3389/fimmu.2021.643771
- Memarnejadian, A., C.E. Meilleur, C.R. Shaler, K. Khazaie, J.R. Bennink, T.D. Schell, and S.M.M. Haeryfar. 2017. PD-1 blockade promotes epitope spreading in anticancer CD8⁺ T cell responses by preventing fratricidal death of subdominant clones to relieve immunodomination. *J. Immunol*. 199:3348–3359. https://doi.org/10.4049/jimmunol.1700643
- Miheecheva, N., E. Postovalova, Y. Lyu, A. Ramachandran, A. Bagaev, V. Svekolkin, I. Galkin, V. Zyrin, V. Maximov, Y. Lozinsky, et al. 2022. Multiregional single-cell proteogenomic analysis of ccRCC reveals cytokine drivers of intratumor spatial heterogeneity. Cell Rep. 40:111180. https://doi.org/10.1016/j.celrep.2022.111180
- Mitra, A., M.C. Andrews, W. Roh, M.P. De Macedo, C.W. Hudgens, F. Carapeto, S. Singh, A. Reuben, F. Wang, X. Mao, et al. 2020. Spatially resolved analyses link genomic and immune diversity and reveal unfavorable neutrophil activation in melanoma. *Nat. Commun.* 11:1839. https://doi.org/10.1038/s41467-020-15538-9
- Nassar, D., M. Latil, B. Boeckx, D. Lambrechts, and C. Blanpain. 2015. Genomic landscape of carcinogen-induced and genetically induced mouse skin squamous cell carcinoma. *Nat. Med.* 21:946–954. https://doi.org/10.1038/nm.3878
- Nguyen, K.B., M. Roerden, C.J. Copeland, C.M. Backlund, N.G. Klop-Packel, T. Remba, B. Kim, N.K. Singh, M.E. Birnbaum, D.J. Irvine, and S. Spranger. 2023. Decoupled neoantigen cross-presentation by dendritic cells limits anti-tumor immunity against tumors with heterogeneous neoantigen expression. *Elife*. 12:e85263. https://doi.org/10.7554/eLife.85263
- Nirmal, A.J., Z. Maliga, T. Vallius, B. Quattrochi, A.A. Chen, C.A. Jacobson, R.J. Pelletier, C. Yapp, R. Arias-Camison, Y.-A. Chen, et al. 2022. The spatial landscape of progression and immunoediting in primary melanoma at

- single-cell resolution. Cancer Discov. 12:1518–1541. https://doi.org/10 .1158/2159-8290.CD-21-1357
- Pelka, K., M. Hofree, J.H. Chen, S. Sarkizova, J.D. Pirl, V. Jorgji, A. Bejnood, D. Dionne, W.H. Ge, K.H. Xu, et al. 2021. Spatially organized multicellular immune hubs in human colorectal cancer. *Cell.* 184:4734–4752.e20. https://doi.org/10.1016/j.cell.2021.08.003
- Reed, J.R., M.D. Stone, T.C. Beadnell, Y. Ryu, T.J. Griffin, and K.L. Schwertfeger. 2012. Fibroblast growth factor receptor 1 activation in mammary tumor cells promotes macrophage recruitment in a CX3CL1-dependent manner. PLoS One. 7:e45877. https://doi.org/10.1371/journal.pone.0045877
- Reeves, M.Q., E. Kandyba, S. Harris, R. Del Rosario, and A. Balmain. 2018. Multicolour lineage tracing reveals clonal dynamics of squamous carcinoma evolution from initiation to metastasis. *Nat. Cell Biol.* 20: 699-709. https://doi.org/10.1038/s41556-018-0109-0
- Ribas, A., and J.D. Wolchok. 2018. Cancer immunotherapy using checkpoint blockade. Science. 359:1350-1355. https://doi.org/10.1126/science.aar4060
- Snippert, H.J., L.G. van der Flier, T. Sato, J.H. van Es, M. van den Born, C. Kroon-Veenboer, N. Barker, A.M. Klein, J. van Rheenen, B.D. Simons, and H. Clevers. 2010. Intestinal crypt homeostasis results from neutral competition between symmetrically dividing Lgr5 stem cells. Cell. 143: 134–144. https://doi.org/10.1016/j.cell.2010.09.016
- Turajlic, S., H. Xu, K. Litchfield, A. Rowan, S. Horswell, T. Chambers, T. O'Brien, J.I. Lopez, T.B.K. Watkins, D. Nicol, et al. 2018. Deterministic evolutionary trajectories influence primary tumor growth: TRACERx renal. Cell. 173:595–610.e11. https://doi.org/10.1016/j.cell.2018.03.043
- Van der Auwera, G.A., and B.D. O'Connor. 2020. Genomics in the Cloud: Using Docker, GATK, and WDL in Terra. First edition. O'Reilly Media, Sebastopol, CA, USA.
- Wang, K., M. Li, and H. Hakonarson. 2010. ANNOVAR: Functional annotation of genetic variants from high-throughput sequencing data. *Nucleic Acids* Res. 38:e164. https://doi.org/10.1093/nar/gkq603
- Westcott, P.M.K., F. Muyas, H. Hauck, O.C. Smith, N.J. Sacks, Z.A. Ely, A.M. Jaeger, W.M. Rideout III, D. Zhang, A. Bhutkar, et al. 2023. Mismatch repair deficiency is not sufficient to elicit tumor immunogenicity. Nat. Genet. 55:1686-1695. https://doi.org/10.1038/s41588-023-01499-4
- Wolf, Y., O. Bartok, S. Patkar, G.B. Eli, S. Cohen, K. Litchfield, R. Levy, A. Jiménez-Sánchez, S. Trabish, J.S. Lee, et al. 2019. UVB-induced tumor heterogeneity diminishes immune response in melanoma. *Cell*. 179: 219–235.e21. https://doi.org/10.1016/j.cell.2019.08.032
- Wong, C.E., J.S. Yu, D.A. Quigley, M.D. To, K.-Y. Jen, P.Y. Huang, R. Del Rosario, and A. Balmain. 2013. Inflammation and Hras signaling control epithelial-mesenchymal transition during skin tumor progression. Genes Dev. 27:670–682. https://doi.org/10.1101/gad.210427.112
- Xie, Z., A. Bailey, M.V. Kuleshov, D.J.B. Clarke, J.E. Evangelista, S.L. Jenkins, A. Lachmann, M.L. Wojciechowicz, E. Kropiwnicki, and K.M. Jagodnik. 2021. Gene set knowledge discovery with Enrichr. Curr. ProtoC. 1. e90. https://doi.org/10.1002/cpz1.90



Supplemental material



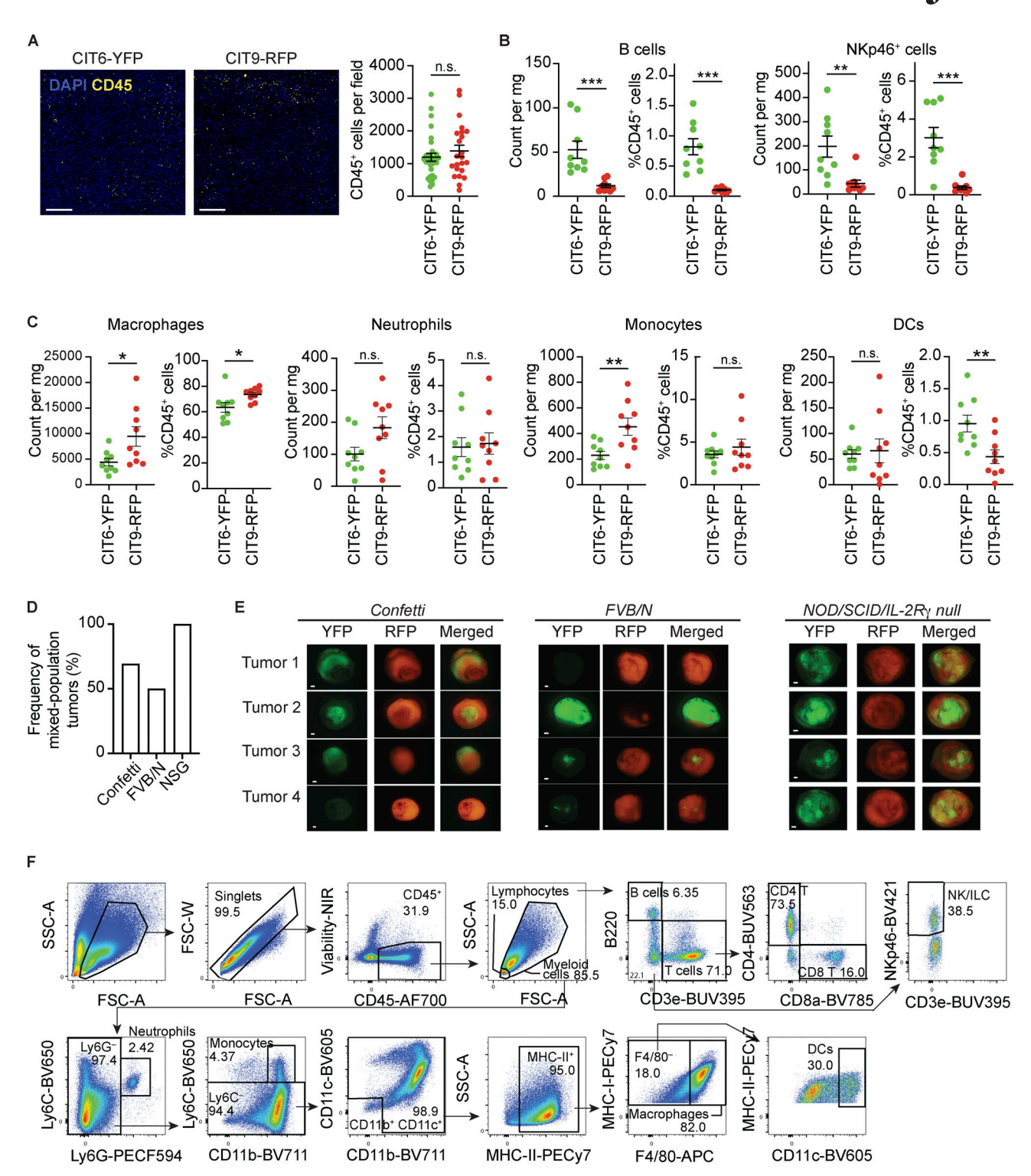


Figure S1. Abundance of immune cell subsets in CIT6-YFP and CIT9-RFP subcutaneous tumors and establishment of mixed tumors. CIT6-YFP and CIT9-RFP tumors were injected into homozygous Confetti mice and harvested at 10 mm for immune cell analysis. (A) Representative image of CD45 stain and quantification of CD45+ total immune cells per field in CIT6-YFP and CIT9-RFP tumors as measured by immunofluorescence staining. CD45+ cells were counted in 31 (CIT6-YFP) and 23 tiles (CIT9-RFP) of a tile scan image. The data are a representation of eight CIT6 tumors and six CIT9 tumors analyzed. Scale bars are 200 μ m. (B and C) (B) Abundance of B cells and NKp46+ lymphocytes and (C) myeloid cell types as measured by flow cytometry. n = 9. The data in B and C presented as count per mg and % CD45+ cells are a representation of one and three independent experiments, respectively. (D and E) (D) Frequency of mixed-population tumors and (E) representative fluorescent stereomicroscope whole-tumor images of mixed-population tumors formed in Confetti, FVB/N, and NOD/SCID/IL-2Ry null mice (n = 12, 8, and 8, respectively). Scale bars in E are 1 mm. The data are a representation of one (FVB/N and NOD/SCID/IL-2Ry null mice) and three (Confetti) independent experiments, respectively. (F) Flow cytometric gating strategy of main immune cell types. Immune analysis of a subcutaneous CIT6-YFP tumor is shown as representative data. Statistical significance was determined by Student's t test in all data. *P < 0.05, **P < 0.01, and ***P < 0.001.



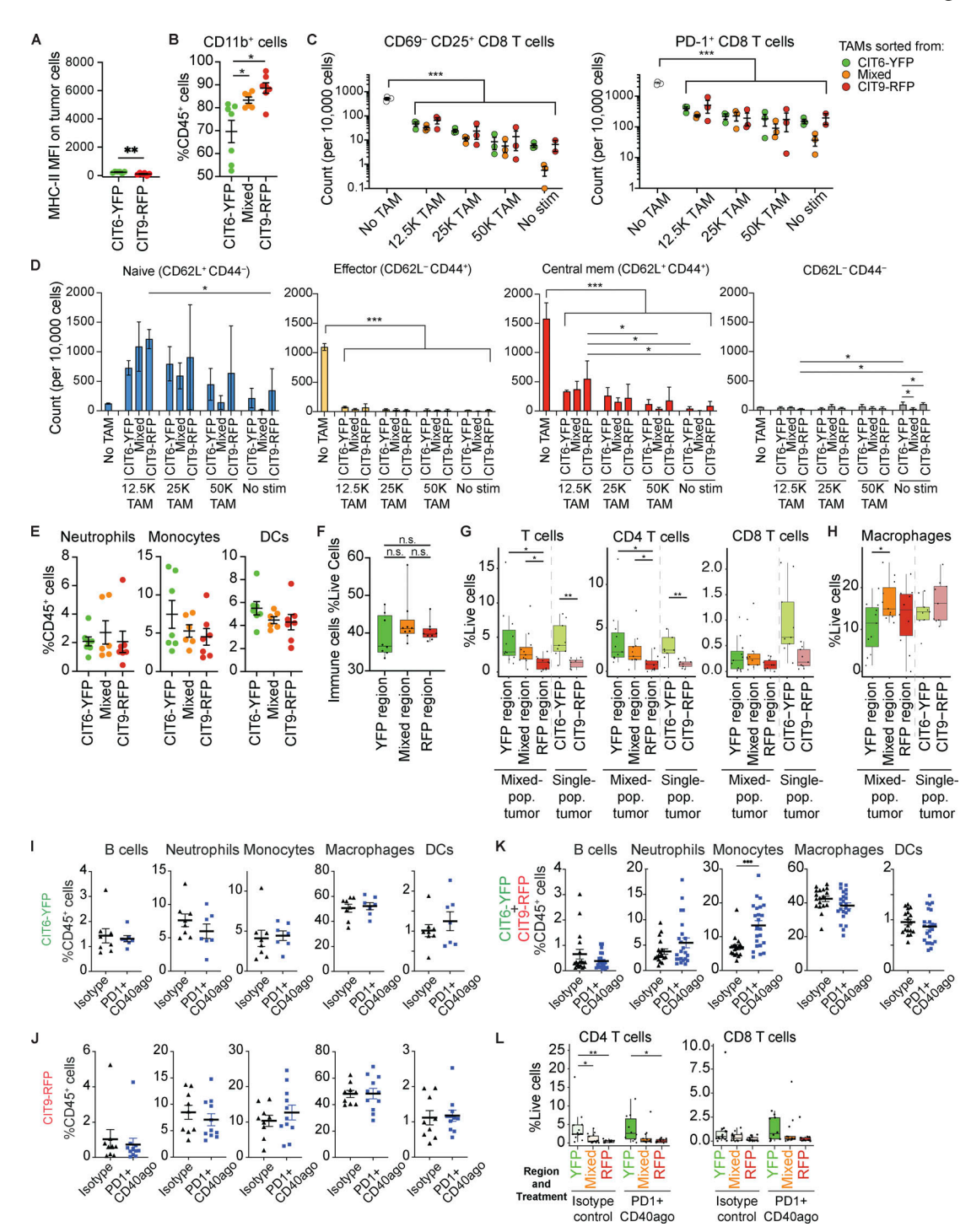


Figure S2. Immune cell infiltration and function in CIT6-YFP, CIT9-RFP, and mixed-population tumors and in tumors treated with PD-1 blockade + CD40 agonist combination therapy. (A) Expression of MHC-II (I-A/I-E) on tumor cells in CIT6-YFP and CIT9-RFP tumors (n = 6). (B) Frequency of CD11b⁺ cells (n = 6-7). (C) Frequency of CD69⁻ CD25⁺ and PD-1⁺-activated T cells in in vitro co-culture assay of CD8 T cells and macrophages sorted from CIT6-YFP, CIT9-RFP, and mixed-population tumors (n = 3). (D) Frequency of Teff subsets broken down by subset to show statistical test results (n = 3). (E) Frequency of neutrophils, monocytes, and DCs (n = 6-7). All data in A–E are a representation of two independent experiments. (F–H) CIT6-YFP + CIT9-RFP mixed-population tumors were microdissected into YFP, mixed, and RFP regions and analyzed for immune infiltration by flow cytometry. (F) Frequency of total CD45⁺ immune cells in each region (n = 8-9). (G) Frequency of total CD3⁺ T cells, CD4 T cells, and CD8 T cells presented as % live cells. (H) Frequency of total macrophages presented as % live cells. Data in G and H are a representation of two independent experiments with ≥ 6 mice per experiment. (I–K) B cells and main myeloid cell populations in (I) CIT6-YFP tumors (n = 7-8), (J) CIT9-RFP tumors (n = 9-11), and (K) CIT6-YFP + CIT9-RFP tumors (n = 18-23). Experiments in I–K were performed once. (L) Total CD4 T cell (CD45⁺ CD3⁺ CD4⁺) and total CD8 T cell (CD45⁺ CD3⁺ CD8⁺) frequencies in each region of isotype control-treated and combination therapy-treated tumors analyzed at day 6 after treatment initiation (n = 10-16). Experiment was performed once. Statistical significance was determined by Student's t test (A and G–L), one-way (B and E), or two-way ANOVA (C, D, and F) with Tukey's correction. *P < 0.05, **P < 0.01, and ***P < 0.001.



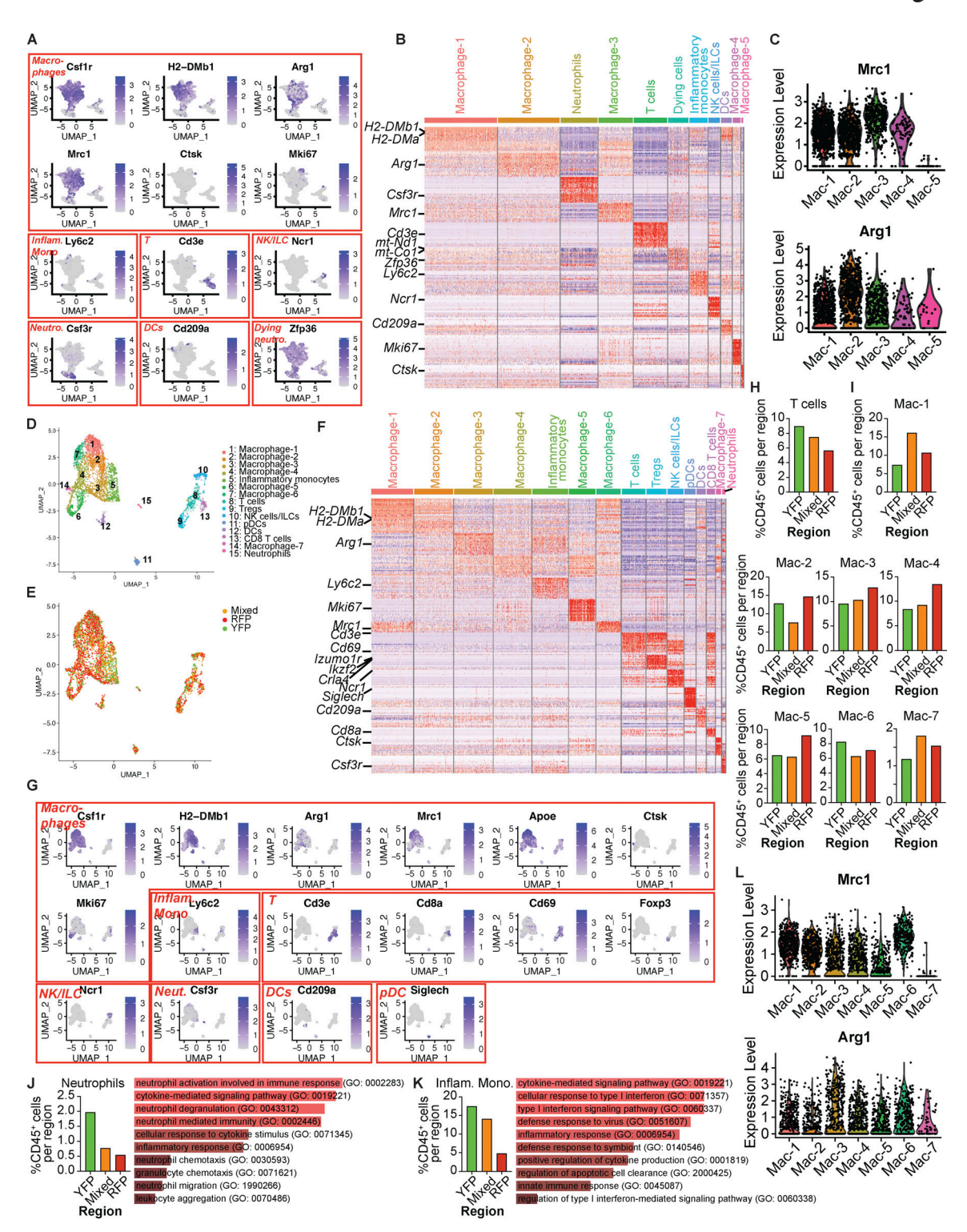


Figure S3. **ZipSeq analysis of mixed-population tumors. (A)** Feature plots overlaid on UMAP representation for *Csfr1*, marking macrophage clusters, and a marker gene for each cluster of the tumor analyzed by ZipSeq in Fig. 6. **(B)** Heatmap showing relative average expression of the 20 most strongly enriched genes for each cluster versus all others for tumor analyzed in Fig. 6. **(C)** Violin plots showing relative average expression of *Mrc1* (CD206) and *Arg1* in Fig. 6. **(D–K)** ZipSeq analysis of a second mixed-population tumor. **(D–E)** UMAP representation of zipcode-labeled cells with (D) cluster overlay and (E) zipcode identity overlay. n = 4,186 cells, $n_{YFP} = 1,015$, $n_{RFP} = 2,011$, and $n_{Mixed} = 1,160$. **(F)** Heatmap showing the 20 most enriched genes in each cluster. Marker gene(s) for each cluster are labeled on the left of the heatmap. **(G)** Feature plots overlaid on UMAP representation for a gene marking macrophage clusters (*Csf1r*) and a marker gene of each cluster. **(H)** Abundance of cells belonging to the T cell cluster, calculated as percentage of total immune cells in each region. **(I)** Abundance of cells belonging to seven macrophage clusters (clusters 1, 2, 3, 4, 6, 7, and 14), calculated as percentage of total immune cells in each region. **(J)** Percentage of cells belonging to the neutrophil cluster (cluster 15) in each region and pathway analysis showing gene families enriched in the neutrophil cluster. **(K)** Percentage of cells belonging to the inflammatory monocyte cluster (cluster 5) and pathway analysis of genes enriched in the monocyte cluster. **(L)** Violin plots showing relative average expression of *Mrc1* (CD206) and *Arg1*. A total of two tumors were analyzed by ZipSeq. ILC, innate lymphoid cell.



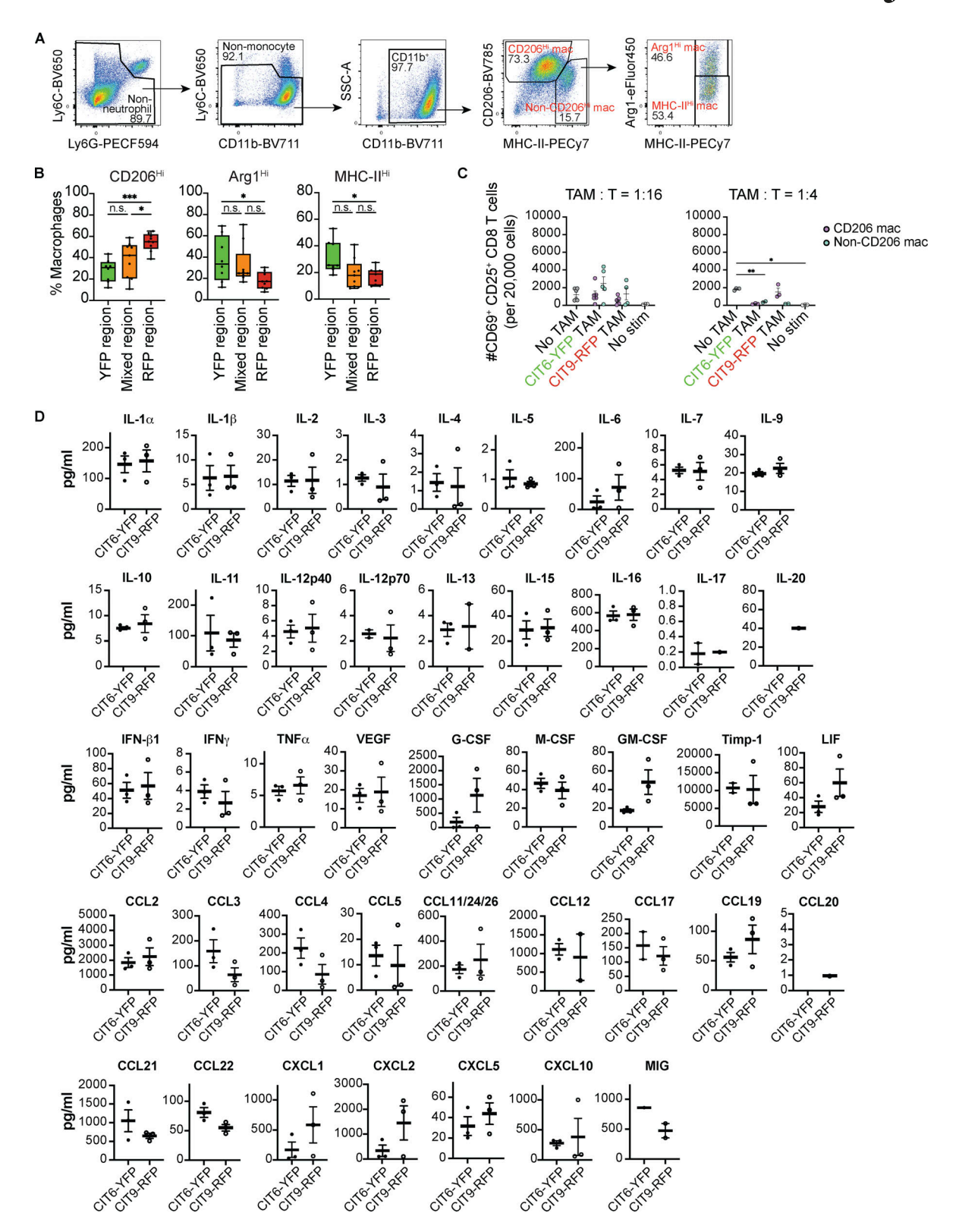


Figure S4. **Spatial and functional analyses of macrophage subsets and analysis of intratumoral cytokines. (A)** Gating strategy identifying MHC-II^{Hi}, Arg1^{Hi}, and CD206^{Hi} macrophage subsets used for flow cytometric analysis and FACS sorting. CD206^{Hi} TAM and non-CD206^{Hi} populations on the fourth plot were used for co-culture T cell suppression assay. Analysis of subcutaneous CIT9-RFP tumor is shown as a representative data. Representation of at least three independent experiments. **(B)** Spatial infiltration pattern of macrophage subsets in mixed-population tumors measured by microdissection followed by flow cytometry, presented as % total macrophages (n = 8-9). The experiment was performed once. **(C)** CD69⁺ CD25⁺-activated T cell count in CD206^{Hi} or non-CD206^{Hi} macrophage–T cell co-culture (1:16 and 1:4 ratios) experiment (n = 3-6). Data are a representation of two independent experiments. **(D)** Protein expression of 43 cytokine and chemokines in CIT6-YFP and CIT9-RFP tumors measured by ELISA (n = 3). Experiment was done once. Statistical significance was determined by one-way ANOVA (B) or two-way ANOVA (C) with Tukey's correction or by Student's t test (D). *P < 0.05, **P < 0.01, and ***P < 0.001.



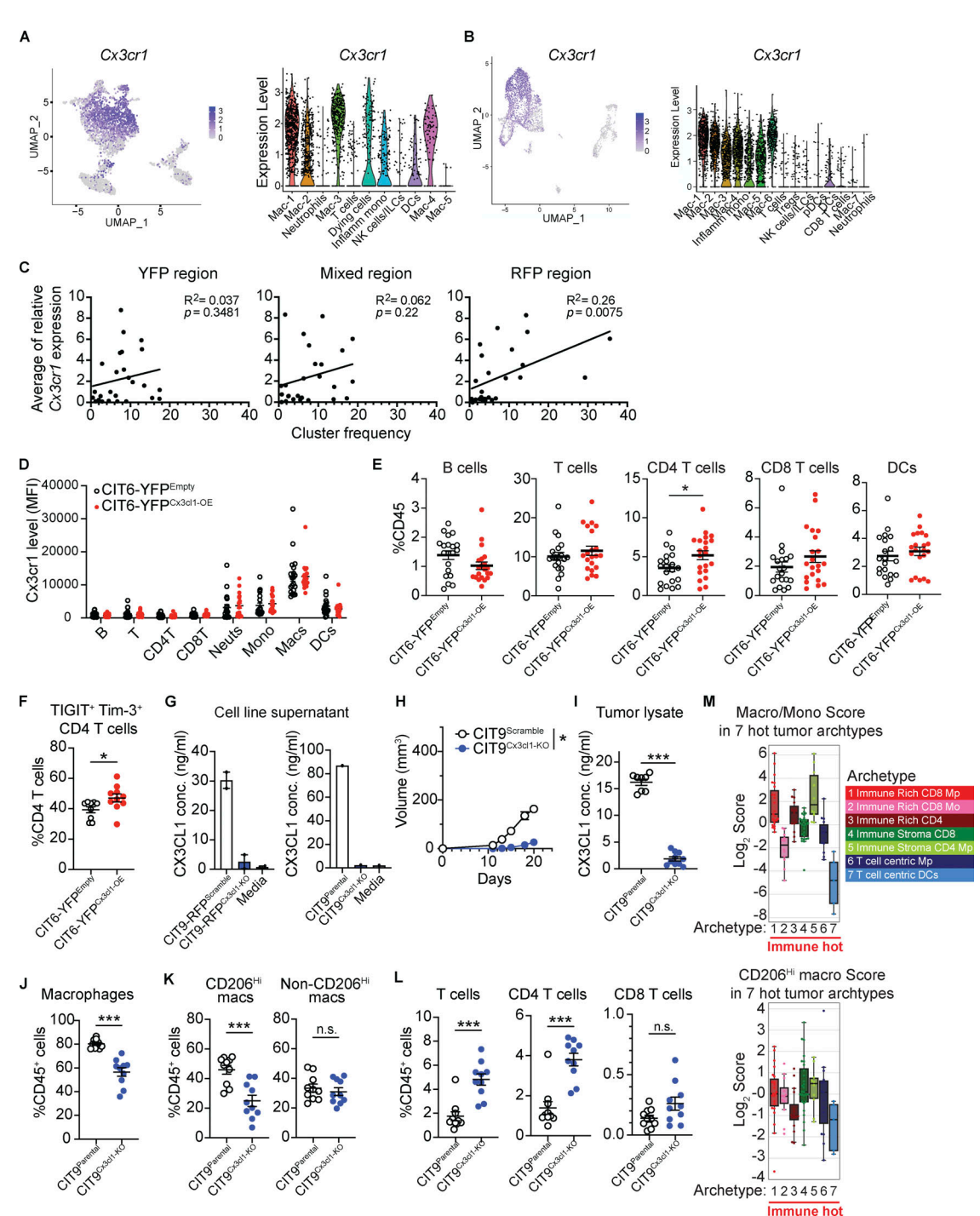


Figure S5. **Effect of Cx3cl1 on tumor-infiltrating immune cells. (A and B)** Feature plots overlaid on UMAP representation for Cx3cr1 and violin plots showing relative average expression of Cx3cr1 of the tumor analyzed by ZipSeq in Fig. 6 (A) and Fig. S3, D-L (B). **(C)** Correlation between an average relative Cx3cr1 transcript level of each cluster and the percentage of cells belonging to the cluster. Combined analysis of two tumors analyzed in Fig. 6 and Fig. S3, D-L. ZipSeq analysis was performed on a total of two tumors. **(D)** MFI of CX3CR1 on major immune cell types in Cx3cl1-overexpressing and empty vector-expressing CIT6-YFP tumors (n = 20-21). **(E)** Frequency of lymphocytes and DCs in Cx3cl1-overexpressing and empty vector-expressing CIT6-YFP tumors (n = 20-21). Data in D and E are a representation of two independent experiments. **(F)** Frequency of TIGIT+ TIM-3+-exhausted CD4 T cells in Cx3cl1-overexpressing and empty vector-expressing CIT6-YFP tumors (n = 9-10). Experiment was done once. **(G)** CX3CL1 concentration in supernatants of Cx3cl1 KO CIT9-RFP cell line (left) and CIT9 cell line (right). Data are an average of two experiments with a total of eight tumors per arm. **(H)** Growth curve of CIT9 parental and CIT9 Cx3cl1 KO tumors (n = 10 per group). **(I)** CX3CL1 concentration in tumor lysate of Cx3cl1 KO CIT9 cells (n = 8-10). **(J-L)** Frequency of total macrophages (J), CD206^{Hi} and non-CD206^{Hi} macrophages (K), and T cells (L) (n = 10). Data in H-L are a representation of two independent experiments. **(M)** Ratio of macrophage score and monocyte score (top) and CD206^{Hi} macrophage score (bottom), based on RNA-seq of mononuclear phagocytes, for human tumors in seven hot immune archetypes (n = 5-28). Statistical significance was determined by Pearson's correlation test (C), one-way ANOVA (E, F, and I-L), two-way ANOVA (H) with Tukey's correction, or by Mann-Whitney test with the Bonferroni correction (M). *P < 0.05 and ***P < 0.001. MFI, median fluorescence intensity;